

DTIC FILE COPY

Lib

# XMR

AD-A229 709

one  
DTIC

1

DEFECTS AND IMPURITIES IN  
MERCURY CADMIUM TELLURIDE

XMR TECHNICAL REPORT TR-88-1B

APRIL 1988

\*Original contains color  
plates. All DTIC reproductions  
will be in black and  
white\*

DTIC  
ELECTE  
NOV 29 1990  
S D<sup>CS</sup> D

RESEARCH SUPPORTED BY IR&D FUNDS OF  
XMR INC. AND IN PART BY DARPA  
UNDER ONR CONTRACT NO. N00014-86-C-0674

EXEMPTION STATEMENT A

Excluded from public release  
Distribution Unlimited

90 11 261

DO NOT REMOVE

\*ZUAAAAAAAAA6902110Z\*

DEFECTS AND IMPURITIES IN HgCdTe



XMR SPECIAL TECHNICAL REPORT TR-88-1B  
March 1988

Research Supported in Part by I.R.&D. funds and in Part by  
Contract No. N00014-86-C-0674

Prepared by:

T. J. Magee and C. Leung  
XMR INC.  
5403 Betsy Ross Drive  
Santa Clara, California 95054

Prepared for:

Dr. R. A. Reynolds  
Dr. J. Murphy  
DEFENSE ADVANCED RESEARCH PROJECTS AGENCY  
1400 Wilson Boulevard  
Arlington, Virginia 22209

Mr. M. N. Yoder  
OFFICE OF NAVAL RESEARCH  
800 North Quincy  
Arlington, Virginia 22217

Accession For	
NTIS	CRA&I <input checked="" type="checkbox"/>
ERIC	TAS <input type="checkbox"/>
Unannounced	<input type="checkbox"/>
Justification	
By	
Distribution /	
Availability Codes	
Dist	Avail and/or Special
A-1	

This document was prepared as a synopsis of work sponsored by an agency of the United States Government. The views and opinions of the authors expressed herein do not necessarily state or reflect those of the United States Government.

UNCLASSIFIED

SECURITY CLASSIFICATION OF THIS PAGE (When Data Entered)

## REPORT DOCUMENTATION PAGE

1a. REPORT SECURITY CLASSIFICATION Unclassified			1b. RESTRICTIVE MARKINGS		
2a. SECURITY CLASSIFICATION AUTHORITY			3. DISTRIBUTION/AVAILABILITY OF REPORT  Approved for public release; distribution unlimited.		
2b. DECLASSIFICATION/DOWNGRADING SCHEDULE N/A					
4. PERFORMING ORGANIZATION REPORT NUMBER(S) XMR-TR-88-1B			5. MONITORING ORGANIZATION REPORT NUMBER(S)		
6a. NAME OF PERFORMING ORGANIZATION XMR Inc.		6b. OFFICE SYMBOL (If applicable)	7a. NAME OF MONITORING ORGANIZATION Office of Naval Research		
6c. ADDRESS (City, State, and Zip Code) 5403 Betsy Ross Drive Santa Clara, CA 95054			7b. ADDRESS (City, State, and Zip Code) 800 North Quincy Arlington, VA 22217		
8a. NAME OF FUNDING/SPONSORING ORG. DARPA		8b. OFFICE SYMBOL (If applicable) DSO	9. PROCUREMENT INSTRUMENT IDENTIFICATION NUMBER N00014-86-C-0674		
8c. ADDRESS (City, State, and Zip Code)  DARPA/DSO 1400 Wilson Blvd., Arlington, CA 22209			10. SOURCE OF FUNDING NUMBERS		
			PROGRAM ELEMENT NO. 63737D	PROJECT NO. 9522	TASK NO. Yd14005
11. TITLE (Include Security Classification)  Defects & Impurities in Mercury Cadmium Telluride (u)					
12. PERSONAL AUTHOR(S) T.J. Magee & C. Leung					
13a. TYPE OF REPORT Scientific	13b. TIME COVERED From: 02/86 TO: 02/88		14. DATE OF REPORT (Year, Month, Day) March 1988		15. PAGE COUNT
16. SUPPLEMENTARY NOTATION					
17. COSATI CODES			18. SUBJECT TERMS (Continue on reverse if necessary and identify by block number)		
FIELD	GROUP	SUB-GROUP	Impurities Etch delineation		
			Mercury Cadmium Telluride Defects		
			Dislocation Lines Digital SIMS		
19. ABSTRACT (Continue on reverse side if necessary and identify by block number) During the past two years, detailed analyses have been performed to address the issue of impurity distribution & clustering in HgCdTe material prepared by LPE, CSVPE, MBE, MOCVD, SSR & THM. This report presents data on comparative analysis of available HgCdTe material, identification of potential sources of impurities, assessment of surface & near-surface regions, & deployment of "dry" cleaning techniques for controlling surfaces & interfaces.					
20. DISTRIBUTION/AVAILABILITY OF ABSTRACT <input type="checkbox"/> UNCLASSIFIED/UNLIMITED <input checked="" type="checkbox"/> SAME AS RPT. <input type="checkbox"/> DTIC USERS			21. ABSTRACT SECURITY CLASSIFICATION UNCLASSIFIED		
22a. NAME OF RESPONSIBLE INDIVIDUAL T.J. Magee			22b. TELEPHONE (Include Area Code) (408) 988-2425		22c. OFFICE SYMBOL

## TABLE OF CONTENTS

<u>SECTION</u>	<u>DESCRIPTION</u>	<u>PAGE</u>
1.0	INTRODUCTION .....	1
2.0	IMPURITIES IN HgCdTe MATERIALS .....	1
3.0	MODEL-DEFECT AND IMPURITY DISTRIBUTIONS IN LPE (VPE) AND MBE (MOCVD) - HgCdTe FILMS .	9
4.0	DIRECT OBSERVATION OF IMPURITY CLUSTER SITES .....	15
4.1	LPE FILMS .....	15
4.2	MBE (MOCVD) FILMS .....	31
4.3	MCT (SUBSTRATE) MATERIAL .....	33
5.0	CHEMICAL ANALYSIS OF IMPURITY CLUSTER REGIONS .....	37
6.0	IMPURITY CLUSTER CORE SITES .....	64
7.0	NON-EQUILIBRIUM THERMODYNAMIC CONSIDERATIONS OF IMPURITY DIFFUSION DURING GROWTH .....	66
8.0	CHARGE STATES AT THE CdTe (HgCdTe) SURFACE IN THE PRESENCE OF RESIDUAL SUBSURFACE DAMAGE AND BURIED IMPURITY CLUSTERS .....	72
9.0	SOURCES OF IMPURITIES .....	78
10.0	IMPURITY INCORPORATION AT SURFACES .....	79
11.0	BINDING OF IMPURITIES TO COMPOUND SEMI- CONDUCTOR SURFACES .....	80
12.0	BINDING OF METALLICS TO COMPOUND SEMI- CONDUCTOR SURFACES .....	86
13.0	SCANNING UV-LASER CLEANING OF SEMICONDUCTOR SURFACES .....	87
14.0	CONCLUSIONS .....	96
15.0	REFERENCES .....	96

# LIST OF FIGURES

<u>FIGURE</u>	<u>DESCRIPTION</u>	<u>PAGE</u>
1	DELINEATED IMPURITY SITES SHOWING STRAIN FIELD REGION AND PARTIALLY REMOVED PRECIPITATE ON GaAs WAFER (REF. 1) .....	4
2	IMPURITY CLUSTER SITES - LEC-GaAs WAFER INTRODUCED FROM SAWING STEP (REF. 1) .....	5
3	MICROGRAPH SHOWING INTERNAL GETTERING OF IMPURITIES ON DISLOCATION LINES IN LP-LEC GaAs (REF. 1) .....	6
4	PHOTOMICROGRAPH OF SSR-HgCdTe SAMPLE (UNANNEALED) SHOWING PRECIPITATION OF IMPURITY CLUSTERS ON DISLOCATION LINES WITHIN SUBGRAIN AND GRAIN BOUNDARIES .....	7
5	PHOTOMICROGRAPH OF LPE-HgCdTe SAMPLE (ANNEALED) SHOWING GETTERING CLUSTERS ON DISLOCATION LINES .....	8
6	SCHEMATIC SHOWING DISTRIBUTION OF DEFECTS/ IMPURITIES IN LPE-HgCdTe EPI-LAYER/ SUBSTRATE SYSTEM .....	10
7	SCHEMATIC SHOWING DISTRIBUTION OF DEFECTS/ IMPURITIES IN MBE (MOCVD) FILMS .....	14
8	REMNAANT SUBSURFACE (SUBSTRATE) DEFECTS PROPAGATING INTO INTERFACE TRANSITIONAL REGION. IMPURITIES ARE PRESENT ALONG LINEAR TRACES AND IN DISCRETE SITES OF TRANSITIONAL ZONE IN EPI-LAYER .....	16
9	REMNAANT DEFECTS IN SUBSTRATE, EXPOSED AFTER STRIPPING EPILAYER .....	18
10	OPTICAL MICROGRAPHS (NOMARSKI MODE) OBTAINED (AFTER DELINEATION) IN NEAR-SURFACE REGION OF CdTe SUBSTRATE SHOWING PRESENCE OF POLISHING INDUCED DRIVE-IN (CLUSTERS) ....	19
11	ETCH DELINEATION OF INTERFACE TRANSITIONAL REGION ( $d \leq 1.8 \text{ } \mu\text{m}$ ) OF LPE FILMS CLUSTERS .....	20
12	IMPURITY CLUSTERS GETTERED ON DISLOCATION LINES IN INTERFACE TRANSITIONAL REGION OF LPE FILM .....	21
13	DISTRIBUTED IMPURITY CLUSTER SITES IN TRANSITIONAL ZONE .....	22
14	LARGE INCLUSIONS AND SMALL DISTRIBUTED IMPURITY CLUSTERS IN INTERFACE TRANSITIONAL REGION .....	23

15	DISTRIBUTED CLUSTERS IN CENTRAL PORTION OF LPE FILM .....	24
16	NUCLEATED CLUSTERS IN CENTRAL PORTION OF LPE-FILM .....	25
17	DISTRIBUTED IMPURITY CLUSTERS .....	26
18	LARGE CONCENTRATION OF IMPURITY CLUSTER SITES IN LOCALIZED REGION WITHIN CENTRAL PORTION OF LPE-FILM .....	27
19	LARGE CONCENTRATION OF IMPURITY CLUSTERS IN CENTRAL REGION OF CSVPE FILM .....	28
20	MICROGRAPHS OF DELINEATED END POINT GROWTH REGIONS OF LPE FILMS .....	29
21	REPRESENTATIVE MICROGRAPHS OBTAINED IN INTERFACE TRANSITIONAL REGIONS OF LPE FILMS ANNEALED FOR 48 AND 96 HOURS .....	30
22	MICROGRAPHS SHOWING THE HIGH CONCENTRATION OF DISTRIBUTED IMPURITY CLUSTERS IN MBE-FILMS .....	32
23	HEAVY CONCENTRATION OF LOCALIZED IMPURITIES IN MOCVD FILM .....	34
24	IMPURITY CLUSTERS IN MOCVD FILM .....	35
25	MICROGRAPHS SHOWING DISTRIBUTION OF GETTERED IMPURITY CLUSTERS IN SUB-GRAIN BOUNDARIES OF SSR-HgCdTe .....	36
26	SECONDARY ION MICROGRAPHS SHOWING GETTERING OF Ti IMPURITY CLUSTERS ON DISLOCATION LINES IN LPE-HgCdTe FILMS .....	38
27	SECONDARY ION MICROGRAPHS SHOWING GETTERING OF Si IMPURITIES ON DISLOCATION LINES IN LPE-HgCdTe FILMS .....	39
28	SECONDARY ION MICROGRAPHS SHOWING GETTERING OF IMPURITIES ON DISLOCATION LINES IN LPE-HgCdTe FILMS .....	40
29	SECONDARY ION MICROGRAPHS SHOWING GETTERING OF IMPURITIES ON DISLOCATION LINES IN LPE-HgCdTe FILMS .....	41
30	SECONDARY ION MICROGRAPHS USING DIGITAL SIMS IMAGING SHOWING Si IMPURITY CLUSTERS ON DISLOCATION LINES IN ADJACENT AREAS OF LPE-FILM .....	42
31	SECONDARY ION MICROGRAPHS SHOWING GETTERING OF IMPURITIES ON DISLOCATIONS IN INTERFACE TRANSITIONAL REGION - LPE-HgCdTe/CdTe .....	43
32	DIGITAL SIMS IMAGING OF Ti IMPURITY CLUSTERS IN ADJACENT AREAS OF LPE FILM ...	44

33	DIGITAL SIMS IMAGING SHOWING PRESENCE OF Si, Fe, Mn, AND Ti CLUSTERS IN SELECTED AREA OF LPE FILM .....	45
34	DIGITAL SIMS IMAGING SHOWING PRESENCE OF Si, Cr, Ti, AND Fe IMPURITY CLUSTERS IN DIFFERENT AREAS OF LPE FILM .....	46
35	DIGITAL SIMS IMAGING OBTAINED SLIGHTLY ABOVE TRANSITIONAL REGION ( $D \approx 3 \text{ um}$ ) CT LPE FILM SHOWING PRESENCE OF Mg, Ti, Si, AND Fe CLUSTERS .....	47
36	DIGITAL SIMS IMAGING OBTAINED ON LPE-HgCdTe/ CdZnTe STRUCTURE PRESENCE OF Si AND Ti AND NEGLIGIBLE Zn CLUSTERS .....	48
37	DIGITAL SIMS IMAGING SHOWING PRESENCE OF Si, Fe AND Ti CLUSTERS IN LPE FILM-100A ..	49
38	DIGITAL SIMS IMAGING SHOWING PRESENCE OF Si AND Ti IN SELECTED AREA OF LPE-FILM-100A .....	50
39	DIGITAL SIMS IMAGING SHOWING PRESENCE OF Si, Fe, AND Ti IN ADJACENT AREA (FIG. 38) OF LPE-FILM-100A .....	51
40	DIGITAL SIMS IMAGING SHOWING PRESENCE OF Mg AND Cr IN AREA OF LPE-FILM .....	52
41	DIGITAL SIMS IMAGING OF Si IMPURITY CLUSTERS IN TRANSITIONAL ZONE OF LPE-FILM .....	53
42	DIGITAL SIMS IMAGING OF Si AND Fe IMPURITY CLUSTERS IN LPE-FILM .....	54
43	DIGITAL SIMS IMAGING OF Si AND Ti CLUSTERS IN LPE-FILM .....	55
44	DIGITAL SIMS IMAGING OF Si CLUSTERS IN SEPARATE AREAS OF LPE FILM .....	56
45	DIGITAL SIMS IMAGING OF CLUSTERS GETTERED ALONG THREADING DISLOCATION LINES OF LPE FILM .....	57
46	DIGITAL SIMS IMAGING OF STEP-ETCHED FILM (FIG. 8) SHOWING PRESENCE OF Mg AND Al ALONG SUBSTRATE REMNANT DAMAGE TRACES PROPAGATING INTO EPI-LAYER AND Si AND Fe IN ADJACENT SITES .....	58
47	DIGITAL SIMS IMAGING OBTAINED ON MBE-FILM SHOWING PRESENCE OF Mg, Fe, Cr CLUSTERS ..	60
48	DIGITAL SIMS IMAGING OBTAINED ON MOCVD-FILM SHOWING PRESENCE OF Mg, Fe, Cr, AND Ti IMPURITY CLUSTERS .....	61
49	DIGITAL SIMS IMAGING OBTAINED ON MOCVD-FILM SHOWING PRESENCE OF Zn, Si, AND Al IMPURITY CLUSTERS .....	62

50	DIGITAL SIMS IMAGING SHOWING PRESENCE OF Mg AND Fe IMPURITY CLUSTERS IN THM- HgCdTe MATERIAL .....	63
51	CLUSTERING IN 48-HOUR 270°C ANNEALED HgCdTe SHOWING HIGH CONCENTRATION OF Si AND PRESENCE OF Te CORE IN CENTRAL PRECIPITATE .....	65
52	DIGITAL SIMS IMAGES OBTAINED ON MOCVD-FILM SHOWING PRESENCE OF Si AND C AND O AS POTENTIAL CORE SITES .....	67
53	OPTICAL MICROGRAPHS (NOMARSKI MODE) OBTAINED ON SAPPHIRE SURFACES AFTER DECORATION SHOWING PRESENCE OF EXTENSIVE BURIED (CHARGED) LINEATED DAMAGE TRACES (REF. 1) .....	74
54	OPTICAL MICROGRAPHS (NOMARSKI MODE) OBTAINED ON LITHIUM NIOBATE SURFACES AFTER DECORATION SHOWING PRESENCE OF EXTENSIVE BURIED (CHARGED) LINEATED DAMAGE AT VARYING DEPTHS ASSOCIATED WITH MULTIPLE POLISHING STEPS (REF. 1) .....	75
55	OPTICAL MICROGRAPHS (NOMARSKI MODE) OF DECORATED SURFACES SHOWING CHARGED STATES ASSOCIATED WITH BURIED DAMAGE AND CLUSTERS (REF. 1) .....	76
56	OPTICAL MICROGRAPH OF DECORATED CdTe SURFACE SHOWING PRESENCE OF CHARGE STATES ASSOCIATED WITH PRESENCE OF BURIED REMNANT DAMAGE AND IMPURITIES .....	77
57	SIMPLIFIED SCHEMATIC SHOWING BONDING OF ORGANIC MOLECULE ONTO COMPOUND SEMI- CONDUCTOR SURFACE .....	82
58	ELECTRONIC CONFIGURATION OF Cd, Te, AND Hg ATOMS .....	84
59	SCHEMATIC SHOWING BONDING OF MOLECULES TO SEMICONDUCTOR SURFACES .....	85
60	BONDING OF IRON OXIDE TO SURFACES .....	88
61	BONDING OF COPPER OXIDE TO SURFACES .....	89
62	BINDING ENTHALPIES OF SINGLE, DOUBLE, AND TRIPLY BONDED STRUCTURES .....	91
63	REPRESENTATIVE INTENSITY PROFILES OF EXCIMER LASER AS A FUNCTION OF POSITION BEFORE AND AFTER HOMOGENIZATION .....	93
64	UV LASER CLEANING OF CdTe SURFACES .....	94
65	SIMS PROFILES OBTAINED ON CdTe "BEFORE" AND "AFTER" UV LASER CLEANING .....	95



## 1.0 INTRODUCTION

Over the past seven years since the initial identification by the authors of defect distributions in CdTe/CdZnTe (CdTe) substrates and epitaxial layers of HgCdTe, improvements in both substrate near-surface quality and defect zoning in epilayers have been noted. Progress in control of impurities and elimination of prominent sources has, however, been almost non-existent.

With the development of new procedures and analytical techniques, impurity zoning in localized regions can now be identified and potential sources isolated. In addition, the deployment of scanning UV-laser cleaning procedures, developed by the authors and used since 1982 for removing particulates and residues from semiconductors, now provides the opportunity for in-situ cleaning of surfaces within the deposition chamber immediately prior to layer growth.

This report provides a brief description of research conducted over the past 2 years on LPE, CSVPE, MOCVD, and MBE - HgCdTe layers deposited on CdTe or CdZnTe substrates including additional research on solid phase regrown HgCdTe, THM material and substrates.

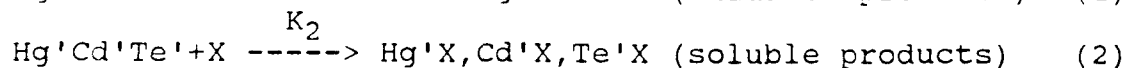
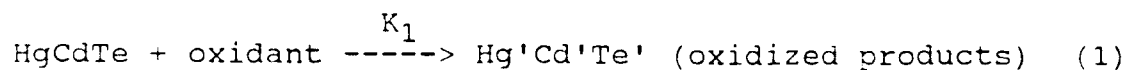
In the sections to follow, we present information obtained on localized impurity clustering in HgCdTe and CdTe material, non-equilibrium diffusion during growth, interaction with distributed defects, core site nucleation centers and potential origin of impurities, including both starting material quality and secondary "system" contributed sources.

## 2.0 IMPURITIES IN HgCdTe MATERIALS

The presence of distributed impurities in CdTe has been suggested from photo-luminescence (PL) measurements. In like manner, DLTS measurements obtained on HgCdTe material have identified the presence of impurities in isolated regions. In all cases, however, the data has been extremely restricted by lack of resolution and a limited range of impurity detection. SIMS profiling measurements obtained in random zones by all laboratories have also shown the presence of impurities in spatially defined regions, but the lack of technology development precluded isolation and consistent analysis of impurity zoning during earlier periods.

The difficulty in finding and localizing impurity sites for standard analytical measurement has been one of the major factors limiting characterization of HgCdTe detector material over the past decade. Unfortunately, this factor has resulted in a failure to identify one of the more significant problems in growth technology and a series of approaches have been implemented that are, in general, inappropriate for improving device yield or materials properties impacting yield.

To expose impurity cluster sites in HgCdTe or CdTe (CdZnTe), we developed controlled etching procedures that would allow the site with the surrounding strain field to be exposed and subsequently examined using scanning electron microscopy (SEM) or optical microscopy (Nomarski mode). The behavior of the reaction involving impurities and chemical etchants on HgCdTe is given by:



where X represents complexing agents and I represents impurities in the HgCdTe matrix.

The actual reaction system is composed of the HgCdTe matrix material, oxidant, complexing agents, and impurities in various chemical states. Since the reaction rates are dependent upon the concentration of both reactant and products, delineation can be controlled by varying concentrations. In this case, the rates of reaction are defined by:

$$R_1 = K_1 [\text{HgCdTe}][\text{Oxidant}] \quad (4)$$

$$R_2 = K_2 [\text{Hg}'\text{Cd}'\text{Te}'][\text{X}] \quad (5)$$

$$R_3 = K_3 [\text{I}][\text{Oxidant}] \quad (6)$$

In normal isotropic etching or dislocation pit delineation, the reaction rates,  $R_1$  and  $R_2$ , are extremely high and material is removed rapidly. However, since the concentration of localized impurities is small compared to the concentration of oxidant, the rate,  $R_3$ , must be carefully controlled, relative to  $R_1$  and  $R_2$ , to expose impurity cluster sites and associated strain fields within the matrix. The

change in the electro-chemical potential within the strain field region also influences reaction rates around the impurity site. Hence, the relative concentrations of complexing agents and oxidant must be adjusted to retain features intact. Furthermore, the solution must be adjusted for changes in alloy composition (X-value), as has been established for dislocation etchants, where  $R_1$  and  $R_2$  are composition dependent.

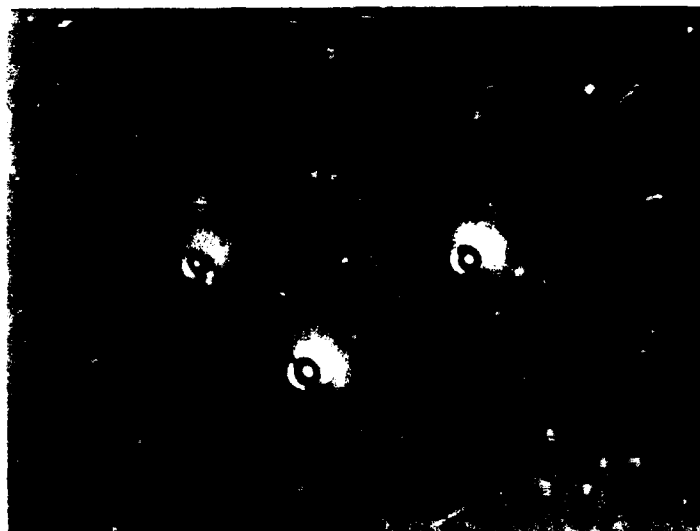
A similar procedure has also been used effectively to isolate and analyze both near-surface drive-in impurities and impurities contained within the bulk of LEC-GaAs crystals. In Figs. 1 and 2 are shown a representative micrographs illustrating the clarity and detail that can be obtained relative to the cluster site. If the etch is terminated in sufficient time, the impurity site can be exposed and the central cluster retained. If etching is continued, the site is removed and a new depth plane will be exposed. Following this procedure we show in Fig. 3 the gettering of impurities along dislocation lines within the bulk of an LEC-GaAs crystal.

For HgCdTe, the solutions are altered and adjusted for variable alloy (X) composition. In Figs. 4 and 5, we show the details of clustering around subgrain boundary regions of HgCdTe and along misfit dislocation lines in the interface transitional region of the LPE HgCdTe film. It can be noted that the relative impurity cluster sizes are variable and many of the smaller sites are located immediately adjacent to dislocation lines in the subgrain boundary regions or along threading dislocations.

To isolate depth zoning regions within HgCdTe films or substrates, we used calibrated stripping (isotropic) solutions and subsequently exposed the surface to the delineation solution. Prior to chemical analysis, the samples were examined in our laser-microscope system. Since the system was designed to allow UV laser irradiation to be focused confocally in the target plane with the HeNe laser light and a broad band visible beam, conventional UV laser cleaning could be used to remove all residue traces and particulates contained on the surface.

Using the indexing system on the Klinger X-Y table, exact coordinates could be determined for impurity cluster location. Using the variable aperture, additional control could be obtained to allow exact positioning of the cluster location.

# Impurity Sites Showing Strain Field Region and Partially Removed Precipitate in Central Region



$200\mu\text{m}$



$100\mu\text{m}$

Fig. 1. Delineated impurity sites showing strain field region and partially removed precipitate on GaAs wafer (Ref. 1)



$50\mu m$

metallics



$50\mu m$

Figure 1. Micrographs of the surface of the metallics after the 100°C anneal.

## Impurity Gettering Along Dislocations in LP-LEC (Undoped) GaAs



Fig. 3. Micrograph showing internal gettering of impurities on dislocation lines in LP-LEC GaAs. Sample was etched to remove 2 mils of material from the surface and subsequently exposed to delineation etch to reveal impurity clusters and surrounding strain fields

100  $\mu m$

0015

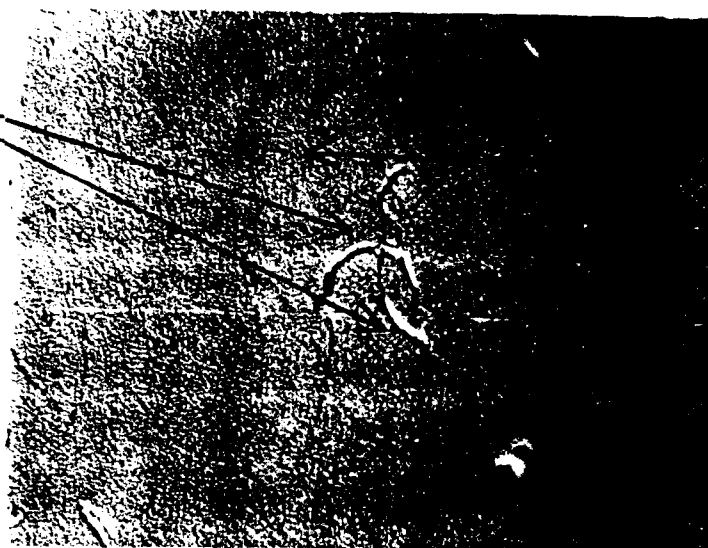
SMALLER  
IMPURITY  
CLUSTERS  
IN SUBGRAIN  
BOUNDARIES



IMPURITY  
CLUSTERS

50 $\mu$ m

SMALLER  
IMPURITY  
CLUSTERS  
IN SUBGRAIN  
BOUNDARIES

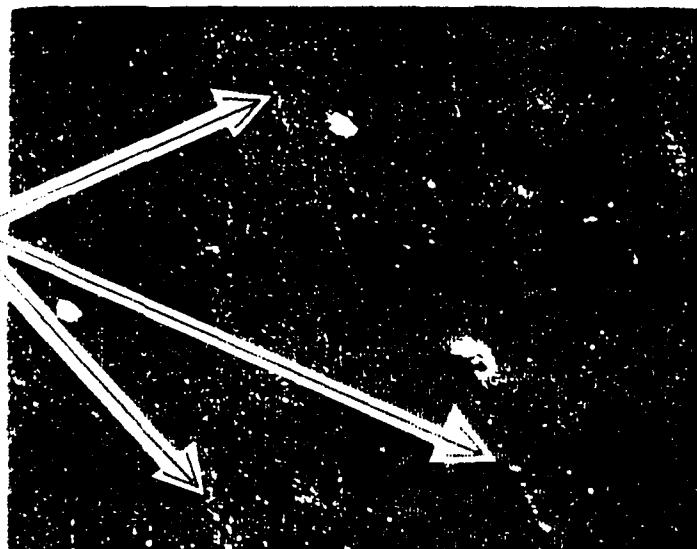


DISTRIBUTED  
IMPURITY  
CLUSTERS

50 $\mu$ m

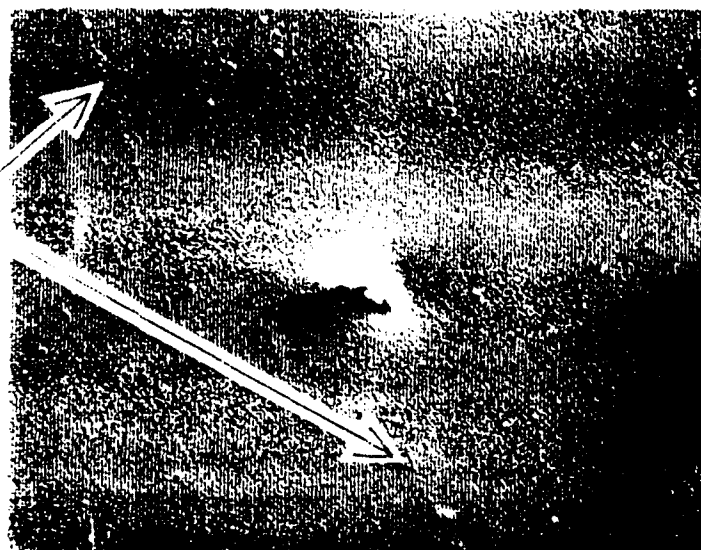
Fig. 4. Photomicrograph of JCB-HgCdTe sample (annealed) showing precipitation of impurity clusters in dislocation loops within subgrain and grain boundaries.

GETTERING  
ON DISLOCATION  
LINES



50  $\mu$ m

GETTERING  
ON DISLOCATION  
LINES



50  $\mu$ m

Fig. 1. Photomicrograph of LPE-HgCdTe sample (annealed) showing gettering clusters on dislocation lines



Since the etch was terminated prior to "opening" of the impurity site, only the strain field region was exposed at the surface. The presence of small protrusions could then be noted with the impurity cluster remaining buried beneath the surface. This procedure allows consistent analyses to be performed within localized areas of the sample.

In the section to follow, we present models of the impurity segregation and defect nucleation zones found in epitaxial HgCdTe films, based on data acquired during the past two years. This will provide a base for discussion of data and allow reference to spatially defined regions of impurity clustering/segregation.

### 3.0 MODEL-DEFECT AND IMPURITY DISTRIBUTIONS IN LPE (VPE) AND MBE (MOCVD) - HgCdTe FILMS

In Fig. 6, we show a schematic of defect and impurity distributions found in LPE (VPE) films. This represents a compilation of data obtained on films examined over the past two years and, as such, is a composite of analytical data obtained on samples from all available sources. The severity of problem areas depicted may indeed vary from film to film. Although the zones are shown as contiguous regions, the most characteristic feature of each is scattered variability. Impurity distributions, nonetheless, are found in all films currently available in the technology area.

Zone 1 is a characteristic end-point region typically displaying variations in composition and surface morphology. Analysis of these regions shows excessive impurity concentrations, line defects and measurable changes in carrier transport properties. This zone has persisted in the technology and few improvements have been noted since the first reports by the authors. Currently, suppliers routinely etch this zone to obtain uniform film properties and to provide uniform surface morphology for processing. In LPE-films, the width of Zone 1 is variable and in MOCVD and CSVPE, variation in surface morphology is the dominant factor.

Zone 2, the interior film region, is characterized by the presence of spatially or laterally varying threading dislocation lines, gettered impurities on dislocation lines and impurity clusters on discrete nucleation sites. Identifiable nucleation core sites include Te and O. In many zones on separate films, the dislocation density (threading) is approximately equal to the substrate dislocation density.

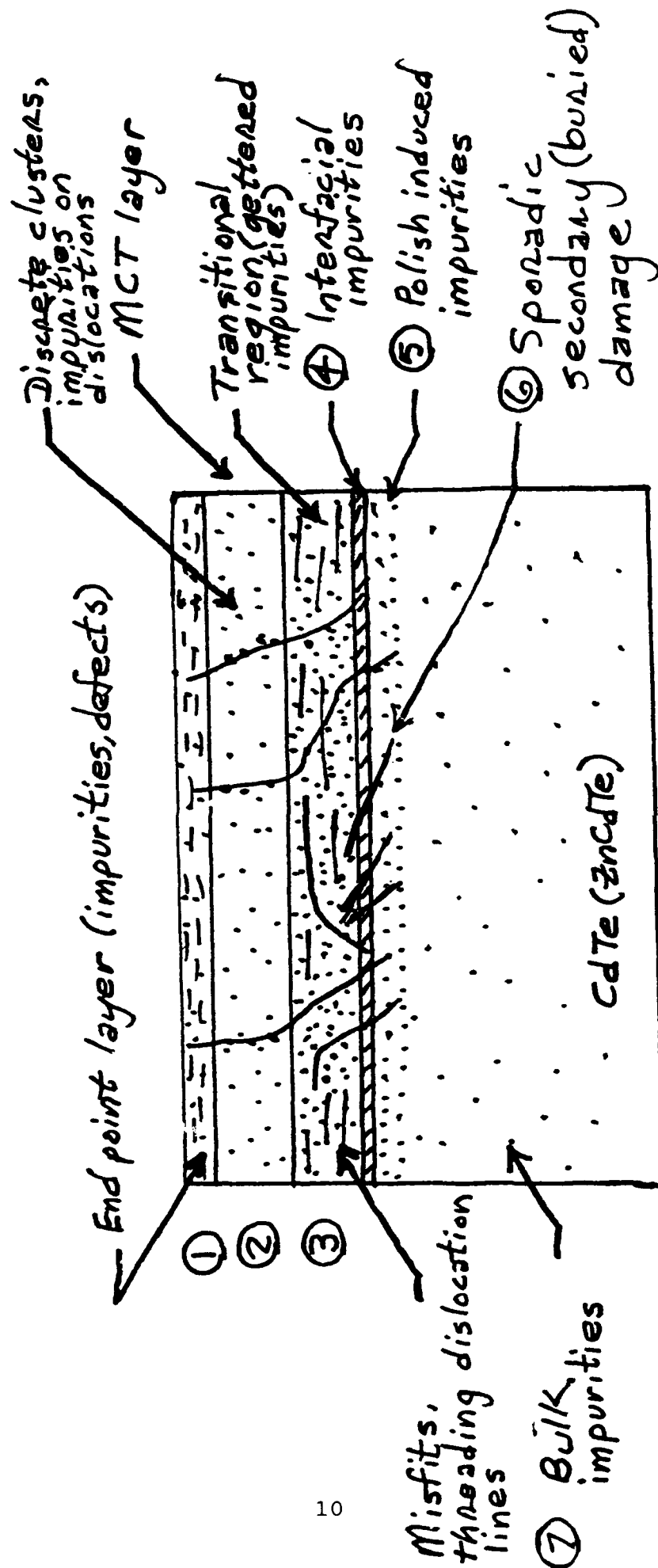


Fig. 6. Schematic showing distribution of defects/impurities in LPE-HgCdTe epi-layer/substrate system

In other zones, the dislocation line density is less than either the interface transitional zone dislocation line density or the substrate density in the adjacent region. This has been discussed in great detail in earlier reports and the current data remains consistent with earlier conclusions.

The interface transitional region, Zone 3, contains misfit dislocations in laterally discontinuous regions, gettered impurities on defects and secondary damage remnants inherited from the substrate. Although the quality and control of substrate near-surface finish has improved, the presence of random (buried) substrate polishing remnant defects remains. Often associated with these sporadic remnant defects are particulates and extraneous impurities introduced during polishing. Also observed in all films examined is an extremely high concentration of impurity clusters either nucleated along line defects or at discrete core sites. The impurity cluster density was always highest in the interface transitional region and typically observed in laterally distributed zones. Twin or subgrain boundaries within the substrate have also been shown to propagate into the epilayer and form very effective gettering sites for impurities within the film. This was not identified as a discrete zone within the epilayers since the boundaries extend throughout the film.

Procedures proposed to control the properties of Zone 3 have included introduction of In doping to compensate defects and impurities or growth of multilayer films of prescribed thickness. In each case, however, these are regarded as tangential or peripheral to the ultimate goal of controlled technology for improved device performance and yield.

The substrate surface (Zone 4) is a source of impurities retained from the cleaning step. This was first identified by the authors in 1983 and subsequently the data has been reproduced by a number of other investigators. Although some improvement has been noted, all the cleaning procedures reported for CdTe, CdZnTe and HgCdTe have failed to produce a "clean" surface suitable for the technology. New developments now offer effective alternative approaches for removing residues, oxides, and particulates (adhering by electrostatic attraction), they will be discussed in a later section.

The substrate near-surface region (Zone 5) contains high concentrations of Cu, Fe, and other impurities. Although the substrate also contains bulk impurities introduced during growth, a finite zone containing high concentrations of depth distributed Cu exceeds the density of bulk Cu impurities. This observed concentration is attributable to a diffusion drive-in mechanism caused by the local temperature increase produced during either ID saw cutting or early stages of pad polishing. The phenomenon is not a new one and has been reported in near-surface regions of Si wafers in 1971 and recently by the authors in GaAs wafers (1983-1987). We have shown within the past year that Cu drive-in is also present in II-VI substrates and can be detected as discrete clusters or gettered sites along secondary remnant damage.

If sufficient material is etched away from the substrate surface, drive-in impurities and remnant damage (Zone 6) are removed. However, in practice, we find that the determination of appropriate removal depths has been empirical and these impurities are present routinely in near-surface regions. In most epitaxial growth systems, the Cu will either diffuse across the interfacial region or be incorporated within the film during melt etchback (LPE).

Although considerable progress has been made in the control of surface finish since the first identification of problem areas and approaches by the authors, sporadic and scattered regions of remnant secondary defects are still detected in the near-surface (substrate) region (Zone 6). These are observed to propagate into the interface transitional regions, producing localized, highly defective regions. Except in the scattered remnant defect regions, distributed areas of excessive particulate (polishing) inclusions are no longer found in the transitional zone.

Within the near-surface region, polish or saw-cut induced drive-in impurities (Zone 5) are typically noted (Cu, Fe). The depth and distribution of these impurities will be dependent upon the level of control in the final polish step and the depth of material removed. When any evidence of sporadic damage is detected within the near-surface region, distributed impurities are always observed, in addition to localized polish solution induced (Mg, Al) concentrations of impurities.

Zone 7 includes the bulk substrate material and provides a source of impurities that has been recognized for some time in LPE layer growth. Unfortunately, the use of alternate substrate material such as CdZnTe has increased the problem of impurity introduction into epilayers. This is attributed to the significant increase in distributed impurities in CdZnTe relative to CdTe.

In MBE/MOCVD films, the distribution of defects and impurities differs substantially from that observed in conventional vapor deposited films. In Fig. 7, we show a schematic of MBE-HgCdTe/CdTe (CdZnTe) and HgCdTe (CdTe)/GaAs structures illustrating results from a compilation of data obtained on available films.

The quality and control of substrate surface finish, in general, appears somewhat better on material from designated suppliers, relative to material from LPE film sources. Although the problem of sporadic defect traces and polish induced impurities is shown in the schematic, this appears only occasionally. Interfacial defects are also observed on HgCdTe/CdZnTe (CdTe) structures with often spatially variable regions associated with irregular nucleation zones. Polycrystalline zones now appear to be related to the retention of residues and/or particulates on the surface.

Growth of CdTe on GaAs has been well documented in studies conducted by the authors and investigators at Rockwell and North Carolina State University and the development of defect zones at the interface has been documented in innumerable, although repetitive, studies conducted subsequently. Research conducted at a much later date on MOCVD-HgCdTe/GaAs also essentially duplicated the previous results, as anticipated.

Hydrocarbon trace residues, impurities and particulates are found on both CdZnTe(CdTe) and GaAs substrates and are not removed by routine cleaning or thermal desorption prior to growth. Such impurities and/or particulates have a noticeable effect on nucleation and defect generation at the interface.

The presence of distributed impurity clusters, often of higher density than a LPE films is routinely noted in MBE and MOCVD layers. These appear to be in bound states and conventional techniques such as photoluminescence or DLTS are totally ineffective for detection. The nature of bonding is currently being investigated, as well as the nucleation or core sites for clustering.

# DEFECT/IMPURITY DISTRIBUTIONS IN MBE(MOCVD) FILMS

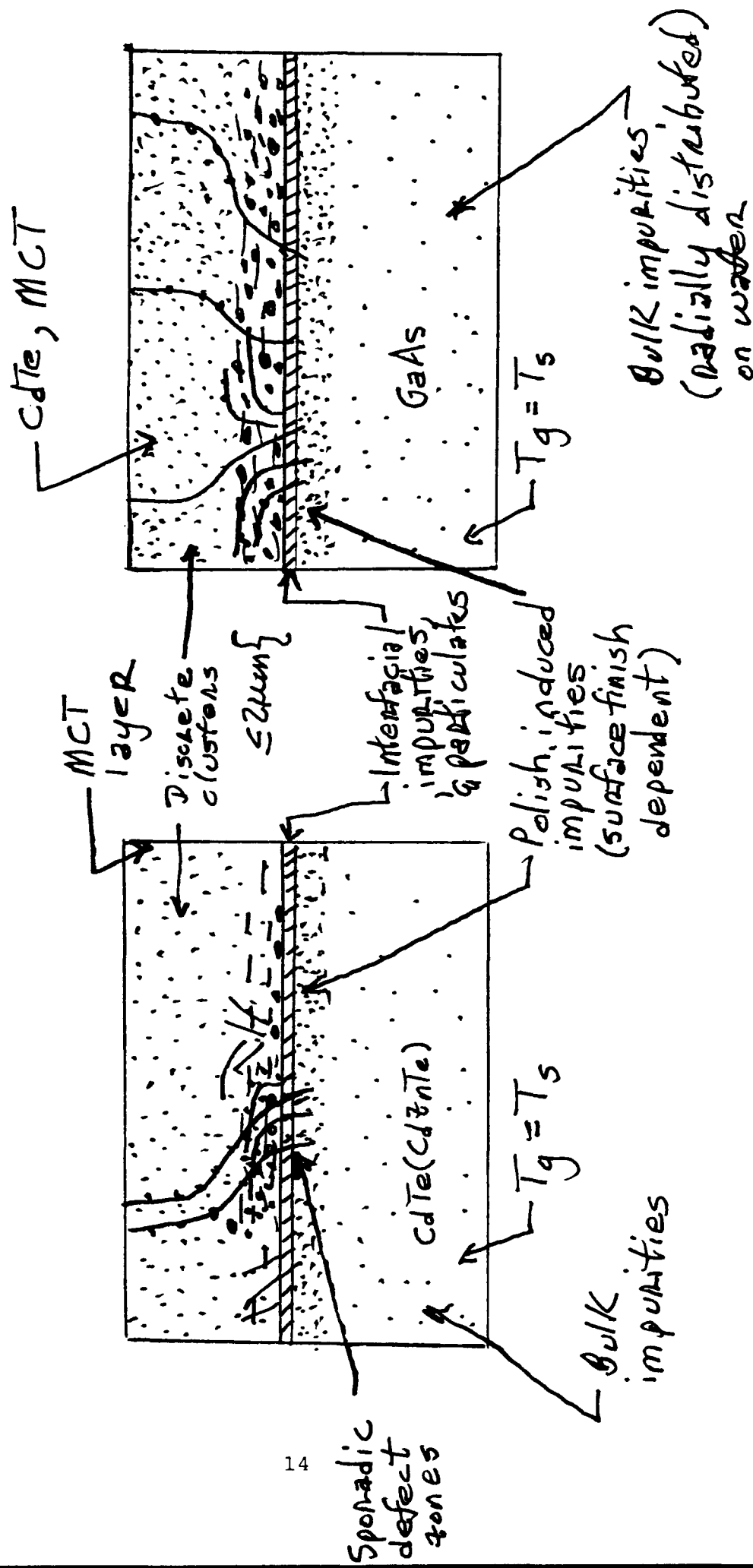


Fig. 7. Schematic showing distribution of defects/impurities in MBE (MOCVD) films

#### 4.0 DIRECT OBSERVATION OF IMPURITY CLUSTER SITES

To expose cluster sites in HgCdTe, we used the selective delineation procedure defined by equations 1-6, and discussed in the previous section. Depth sections were obtained by stripping to controlled depths and subsequently delineating. Examination was then performed using either SEM or optical microscopy (Nomarski mode). To provide additional information on smaller clusters, samples were prepared for TEM analysis by selecting zones exhibiting a noticeable concentration of unexposed cluster sites. The samples were placed on a grid to retain the cluster regions and subsequently exposed to a 3 stage ion milling process at LN<sub>2</sub> temperature. The precipitates were then preserved intact for analysis in the STEM. Alternate procedures will not, in general, reveal or locate impurity zones and are deemed inappropriate for precise localization of spatially distributed clusters.

#### 4.1 LPE FILMS

To isolate regions within the substrate, near-surface region and the interface transitional region, samples were first isotropically stripped with a dissolution etch to leave a thin ( $\leq 2$   $\mu$ m) film on the substrate. The sample was then masked with wax and etched again, exposing a "step" at the substrate/film boundary, as shown in Fig. 8. After exposure to the cluster delineation etch, the sample clearly shows the presence of residual secondary damage structure that has been retained in the near surface region of the substrate. This line damage propagates into the interface transitional region of the film and associated impurities (Al, Mg) are detected along damage traces in the film. Also of interest is the presence of cluster sites in adjacent regions within discrete sites or along dislocation line regions contained within the transitional zone.

In separate samples, we stripped epitaxial layers to reveal the near-surface region of the substrate. In Fig. 9 is shown a representative micrograph illustrating the concentration of fine, distributed line structure retained as buried damage in sporadic or scattered regions of substrates.

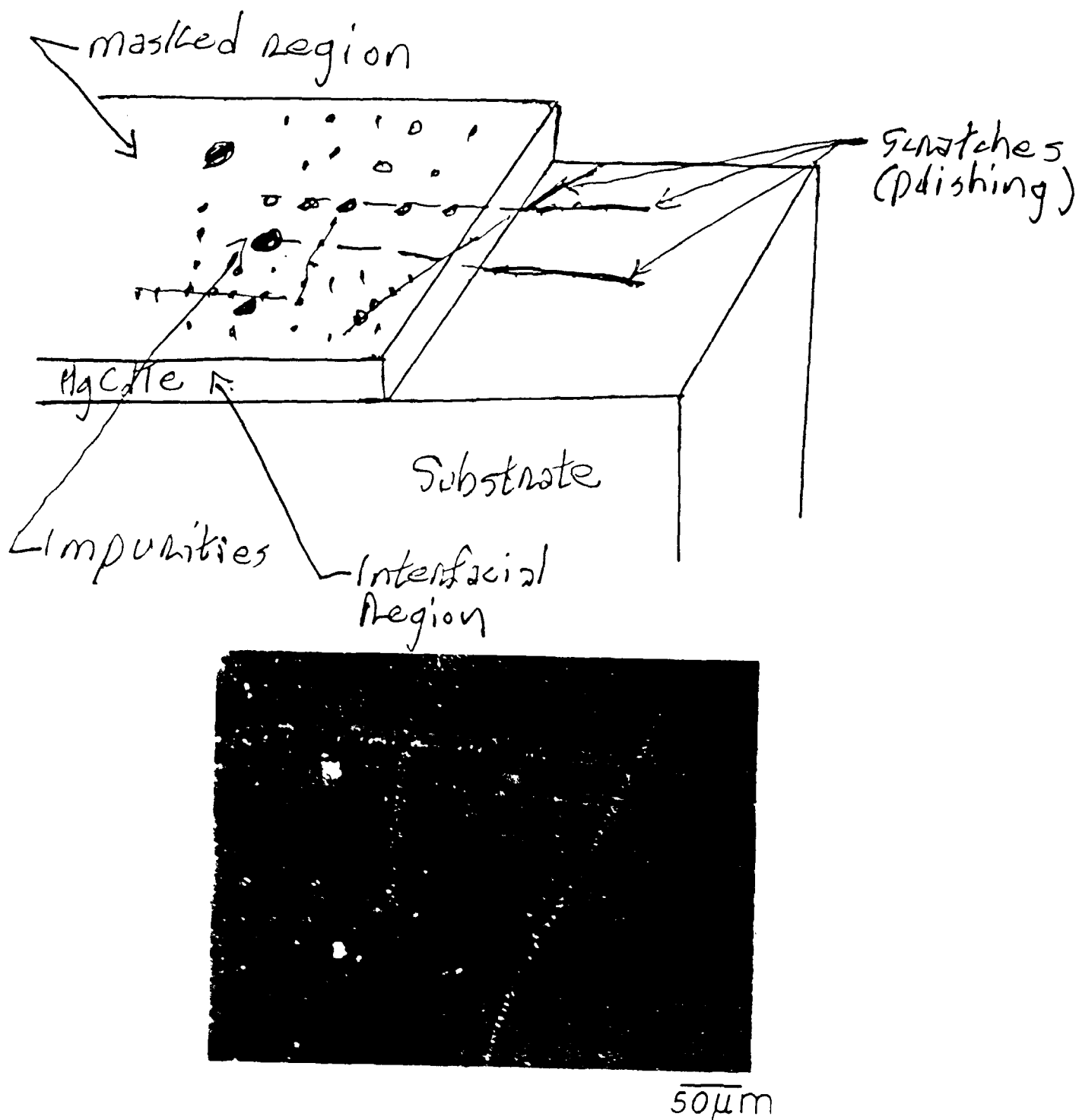


Fig. 3. Remnant subsurface (substrate) defects propagating into interface transitional region. Impurities are present along linear traces and in discrete sites of transitional zone in epi-layer.



Delineation etching of near-surface regions of substrates (Fig. 9) shows impurity clusters associated with polishing or saw-cut induced drive-in diffusion. Impurities pinned along secondary line defects and in discrete sites can be readily detected in Fig. 10. If sufficient material is removed, only discrete impurity clusters are observed and high concentrations of Cu are typically monitored in buried cluster sites.

Within interface transitional zones, we observe the highest concentration of metallic clusters. These tend to be gettered along dislocation lines or distributed sites in the interfacial region. Figures 11-14 are representative micrographs showing the presence of spatially distributed impurity clusters in this region. Within some films, we have noted scattered zones of higher impurity nucleation, typically within regions where excessive meltback has occurred or in areas where higher concentrations of threading or misfit dislocation lines are detected. Within the same film, we cannot resolve clearly defined regions of impurity clustering in some areas of the transitional zone, reflecting the degree of spatial inhomogeneity that can exist.

Within the central regions of LPE-films (Zone 2), the concentration of impurity cluster sites is more evenly distributed (Figs. 15-17). In some zones, however, large concentrations of localized impurities can be detected (Figs. 18 and 19).

The end-point growth region (Zone 1) has been well-characterized in the past, both by the authors and other independent laboratories, and has been shown to contain zones of variable stoichiometry, defects, holes, irregular surface topography, and dislocation lines. Delineation etching of this region also shows high concentrations of impurities (Fig. 20) as anticipated. Normally, this zone is etched away (2  $\mu\text{m}$  - 10  $\mu\text{m}$ ) to eliminate problems in fabrication.

The influence of annealing can be readily observed within LPE films by the increase in concentration of impurity clusters. Within the interface transitional region where dislocation lines are available as gettering sites, we note a marked increase in the number of clusters. In Fig. 21, we show representative micrographs obtained within the transitional region of samples annealed in a Hg-ambient for 48 hours and 96 hours. Counts of clusters across the entire sample plane

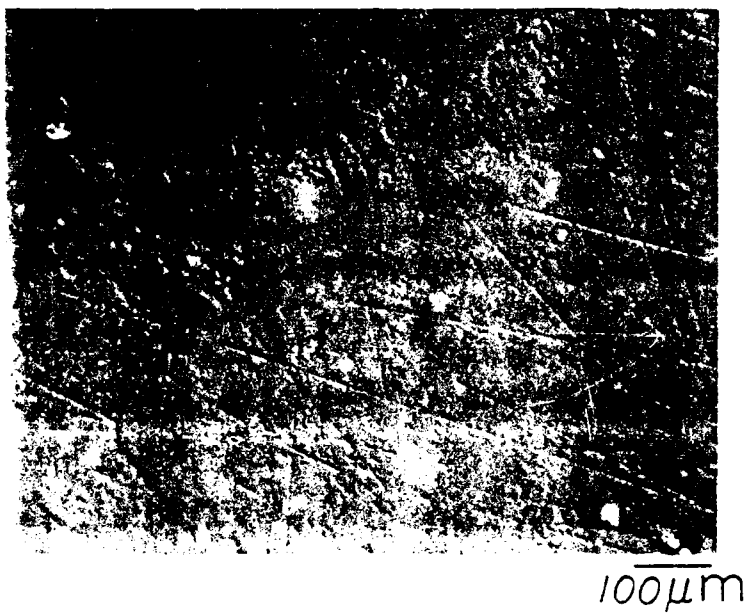
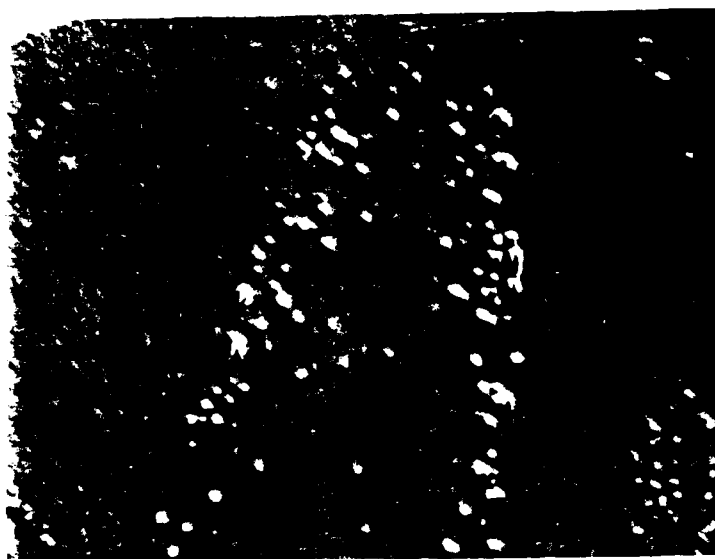


Fig. 2. Remnant defects in substrate, exposed after stripping epi-layer.

0040

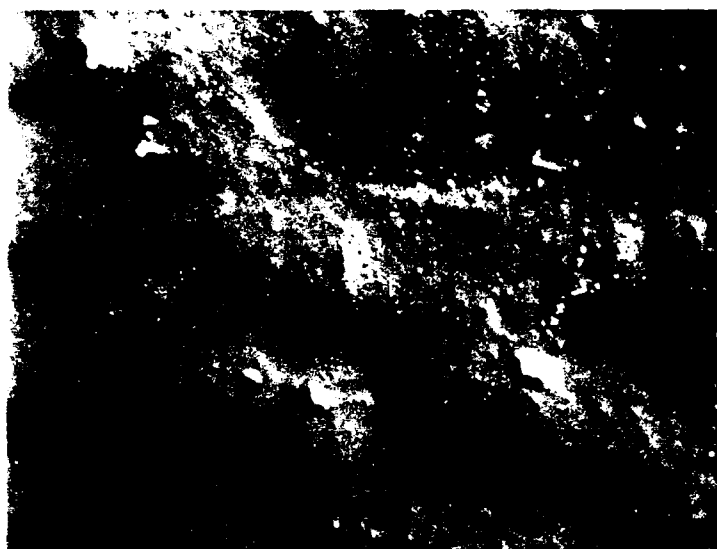


$50\mu\text{m}$



$50\mu\text{m}$

Fig. 10. Optical micrographs (Nomarski mode) obtained (after delineation) in near-surface region of CdTe substrate showing presence of polishing induced drive-in (clusters).



$50\mu\text{m}$

Fig. 11. Etch delineation of interface transitional region  
( $d \leq 1.8 \mu\text{m}$ ) of LPE films clusters

0042



$50\mu m$

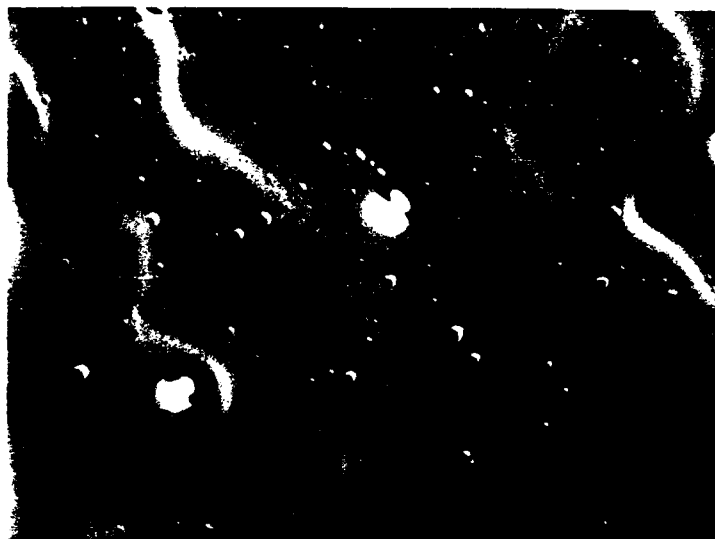
Fig. 12. Impurity clusters getterred on dislocation lines in interface transitional region of LPE film

0043



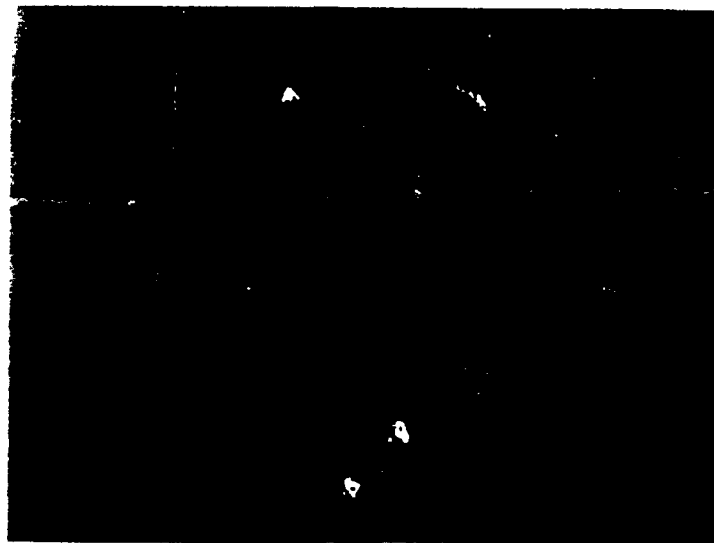
$100\mu m$

Fig. 12. Distributed impurity cluster sites in transitional zone



$100\mu\text{m}$

Fig. 14. Large inclusions and small distributed impurity clusters in interface transitional region



100  $\mu$ m



100  $\mu$ m

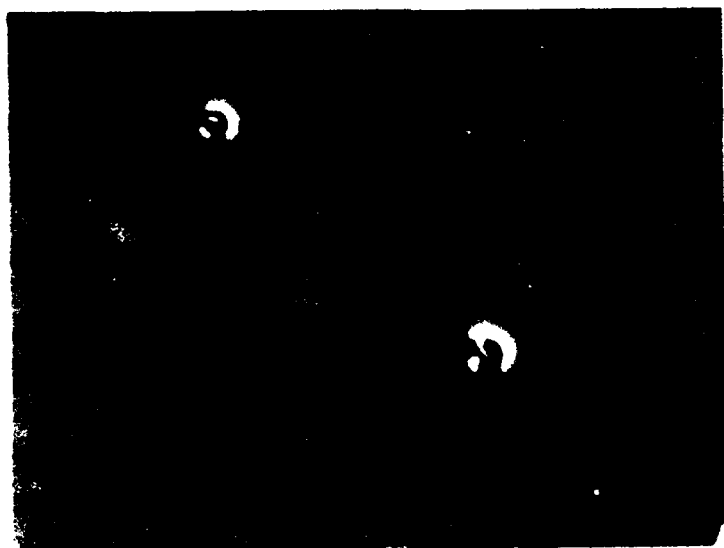
Figure 1. Micrographs of control section of 100  $\mu$ m





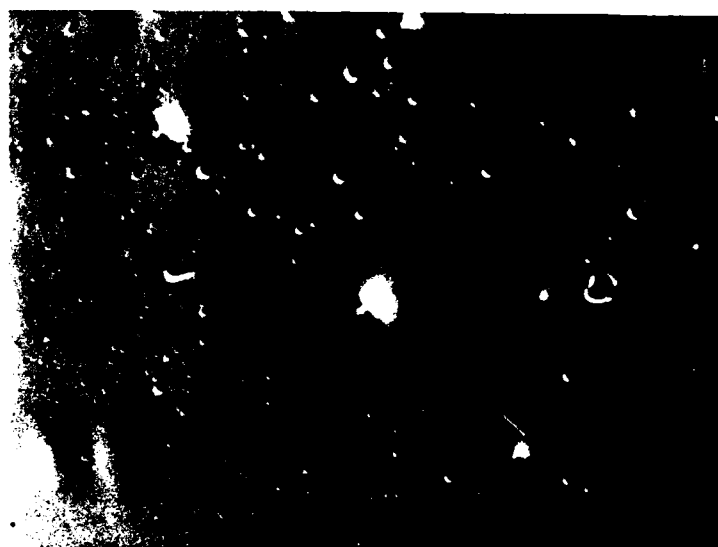
$100\mu\text{m}$

Fig. 16. Nucleated clusters in central portion of LPE-film



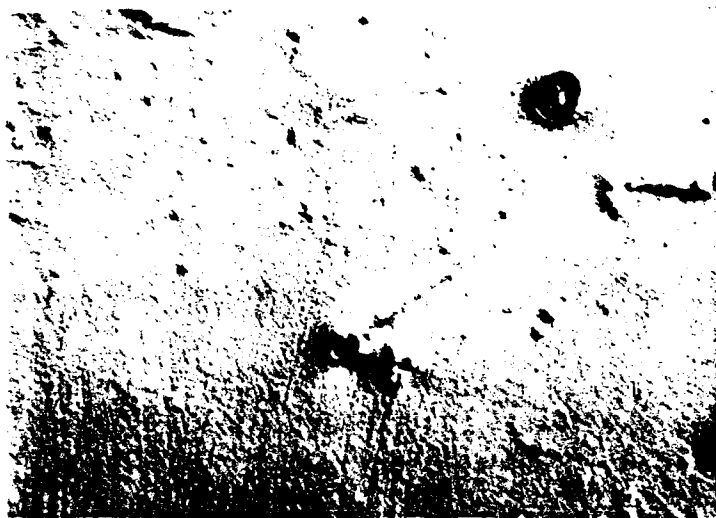
$100\mu m$

Fig. 17. Distributed impurity clusters



$100\mu\text{m}$

Fig. 18. Large concentration of impurity cluster sites in localized region within central portion of LPE-film

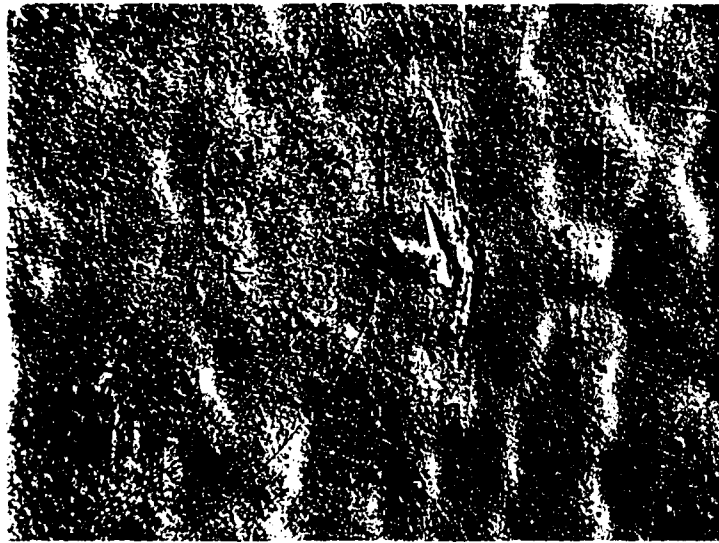


$100\mu\text{m}$

Fig. 19. Large concentration of impurity clusters in central region of CSVPE film

.. 0050

# Impurities in End Point Region LPE - HgCdTe



100  $\mu$ m



100  $\mu$ m

Fig. 20. Micrographs of delineated end point growth regions of LPE films

0051

48 hrs.



$100\mu\text{m}$

96 hrs.



$100\mu\text{m}$

Fig. 21. Representative micrographs obtained in interface transitional regions of LPE films annealed for 48 and 96 hours

0052

show an 85% increase in concentration after 96 hours of annealing. In regions of large concentrations of core or nucleation sites, long diffusion lengths are not required since localization within zones is already attained prior to annealing.

In contrast, films grown by MBE exhibits a high concentration of clustered or bound impurities prior to any external annealing. This can be attributed to a process of in-situ annealing related to the fact that substrates are maintained at a sufficient temperature during growth to provide thermal activation or movement of impurities into sites during deposition. Also, during deposition, sufficient surface mobility exists of impinging impurity atoms to move efficiently into localized regions.<sup>2,3</sup> Although not all impurities are moved into core sites, and many will remain electrically active, the current procedures allow us to analyze the type and concentration of impurities present, independent of growth technique.

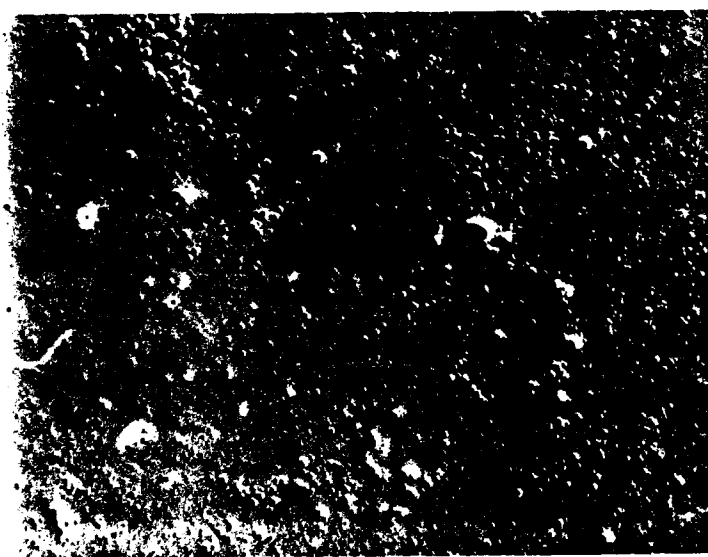
#### 4.2 MBE (MOCVD) FILMS

In contrast to the highly structured or zonal character of impurity distribution in LPE layers, MBE and MOCVD films are rather distinctive in exhibiting a high density, somewhat uniform, distribution of impurities throughout the entire film thickness. Although scattered or localized concentrations of impurities are also found in the substrate/film interface region and along dislocation lines, well-defined layered regions of high impurity concentration within the interfacial region are not detected.

In MBE films, a high concentration of smaller distributed metallic cluster sites is observed, as shown in Fig. 22. From both SEM and TEM data, the results typically show smaller and dispersed regions of impurity nucleation. Although the types of impurities are often similar to those found in LPE films, the abundance of Cr, Fe, and Ti strongly suggests a predominant source mechanism for introduction. The exact description of a source mechanism will require additional studies of films grown in dissimilar systems under varying growth conditions and research in this respect is continuing.



$100\mu\text{m}$



$100\mu\text{m}$

Fig. 12. Micrographs showing the high concentration of distributed impurity clusters in MBE-films

0053



In films grown by MOCVD, we have seen perhaps the highest concentration of distributed impurities of any of the samples examined. Figures 23 and 24 are representative micrographs showing an extremely high concentration of clusters of varying sizes present at approximately the central region of the film. The MOCVD films differ from the MBE films in exhibiting both a higher concentration of clusters and a wider range of impurity species.

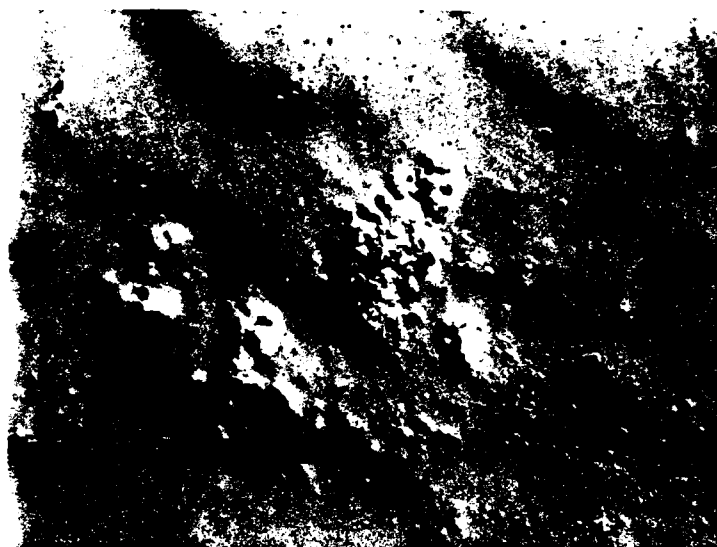
#### 4.3 MCT SUBSTRATE MATERIAL

Material grown by the solid state recrystallization technique (SSR) and the traveling heater method (THM) was provided for comparative analysis. Samples were etched to remove approximately 2 mils of material to avoid any overlap with polishing induced drive-in impurities within near-surface regions. After delineation, samples were examined by optical or scanning electron microscopy.

Material grown by the SSR technique typically exhibited impurity clusters within subgrain boundary regions and in the interior of grains (Fig. 25). Subgrain boundary regions, however, were generally the dominant gettering site for impurities.

Examination of THM samples provided by TI shows only a small number of observable impurity clusters in selected regions of the samples. To further examine volume distributions of impurities in HgCdTe grown by THM technique, we potted cross-sections in a Sn-Bi alloy, subjected the samples to a non-contact polishing process and then exposed the cross sectioned faces to an impurity cluster delineation etch. Only a small number of clusters were detected across the cross sectional faces. Examination of additional sections yielded essentially identical results.

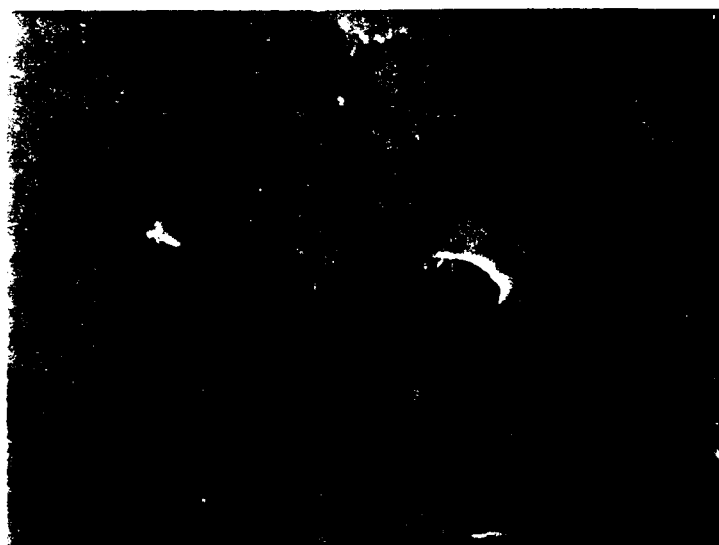
Although only a limited quantity of THM material has been examined thus far, the lowest concentration of metallic clusters revealed by the etch delineation procedure was found in the THM material. During this time, THM material from Europe was also not available, precluding comparison of material prepared in the United States and Europe. Additional tests and comparative studies are currently ongoing to additionally characterize the THM material.



$50\mu m$

Fig. 13. Heavy concentration of localized impurities in HgCdTe film

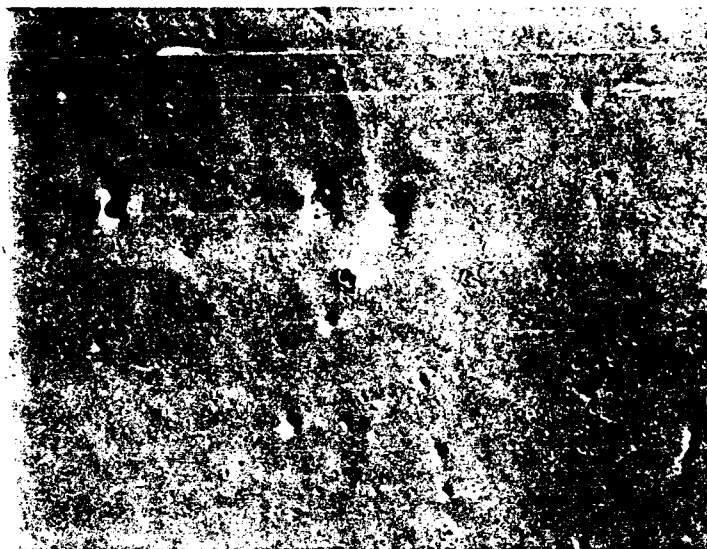
0054



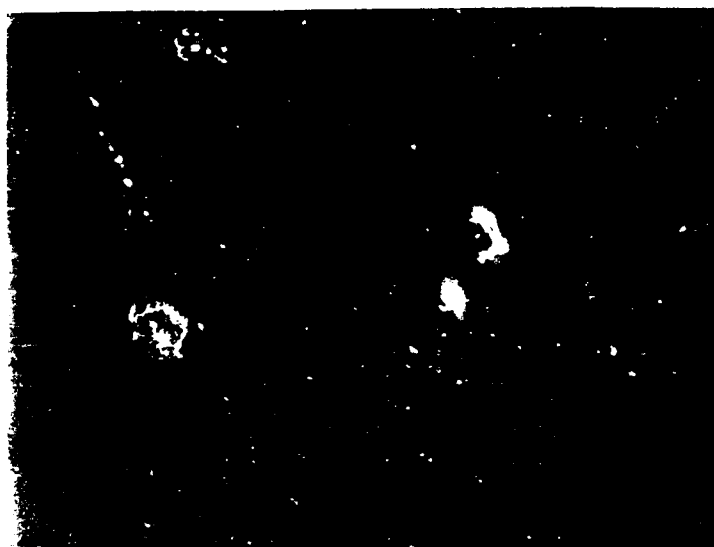
$50\mu\text{m}$

Fig. 24. Impurity clusters in MOCVD film

# Impurity Clusters in Subgrain Boundaries SSR - HgCdTe



$100\mu\text{m}$



$100\mu\text{m}$

Fig. 25. Micrographs showing distribution of gettered impurity clusters in sub-grain boundaries of SSR-HgCdTe

## 5.0 CHEMICAL ANALYSIS OF IMPURITY CLUSTER REGIONS

To provide an analysis of the constituents within impurity cluster regions, we used digital SIMS imaging along with SAD and EDAX analyses in the STEM. After etch delineation, sample surfaces were cleaned using scanning UV cleaning in the UV laser microscope. Regions of cluster concentration were then indexed on the stage of the microscope using axes parallel to the edges of the sample.

Index positions were then used to locate zones on the sample using the stage drive contained on the SIMS unit. An optical telescope was also used to visually locate zones contained on sample surfaces within the SIMS sample chamber. In all cases, only regions containing slightly elevated (closed) features (strain field region) with the cluster buried beneath the surface were examined. This procedure allows localization and analysis of impurity clusters to be made.

The digital SIMS reconstruction in Fig. 26 shows the localization of Ti impurity clusters along dislocation lines in an LPE layer. In this case, propagation of a grain boundary from the substrate into the epilayer is noted and impurity pinning occurs along defects associated with the boundary.

In Figs. 27-30, we observe gettering of Ti, Si, Fe, and C along dislocation lines in LPE layer material. Within the interface transitional region, impurities are also noted along dislocation lines (Fig. 31) and in discrete sites within the interior of the film. The secondary ion micrographs shown in Figs. 32-45 also show the presence of Fe, Mn, Mg, Si, Cr, and Ti impurities in specified regions of LPE films obtained throughout the industry. Other micrographs also show varying amounts of O, C, and Cu. Analyses using EDAX within the STEM also shows the presence of Cu, Fe, and Ni in identifiable cluster or precipitate sites. Selected area diffraction (SAD), however, was not possible because of the thickness of the precipitate clusters and bonding states remain unidentified.

To identify clusters or precipitates associated with remnant damage inherited from the substrate and propagating into the epitaxial layer (Fig. 6), we used the masked and stripped sample (Fig. 8) discussed earlier. Digital SIMS imaging (Fig. 46) shows concentrations of Mg and Al within the substrate and interface transitional zone of the epilayer.

# Secondary Ion Micrographs Showing Gettering of Ti Impurity Clusters on Dislocation Lines in LPE-HgCdTe Film:

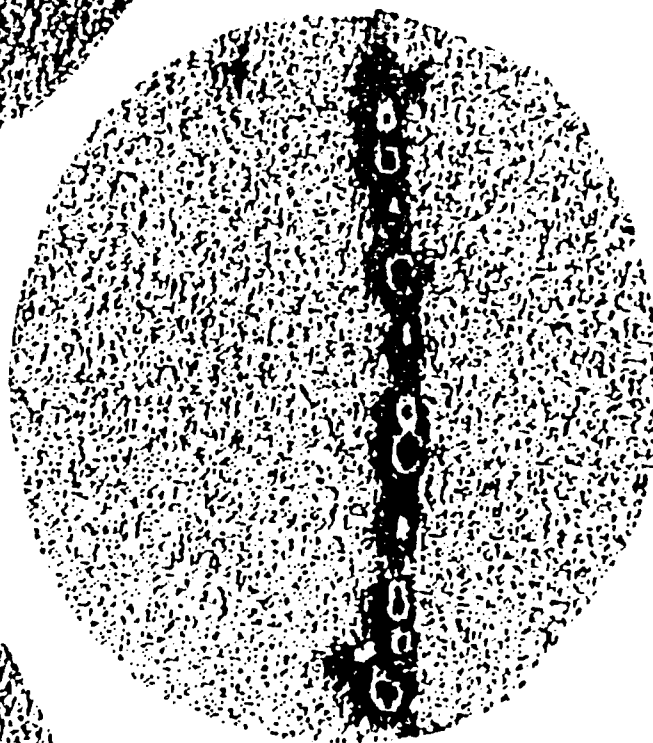
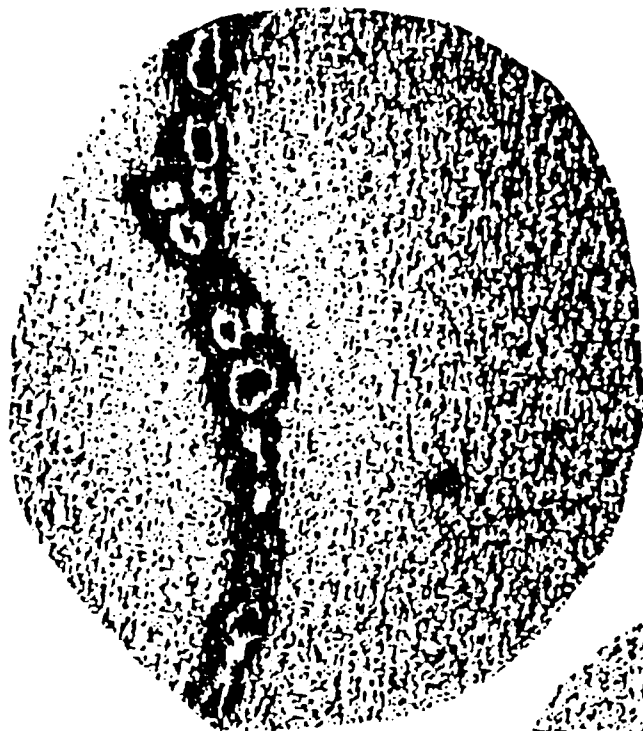
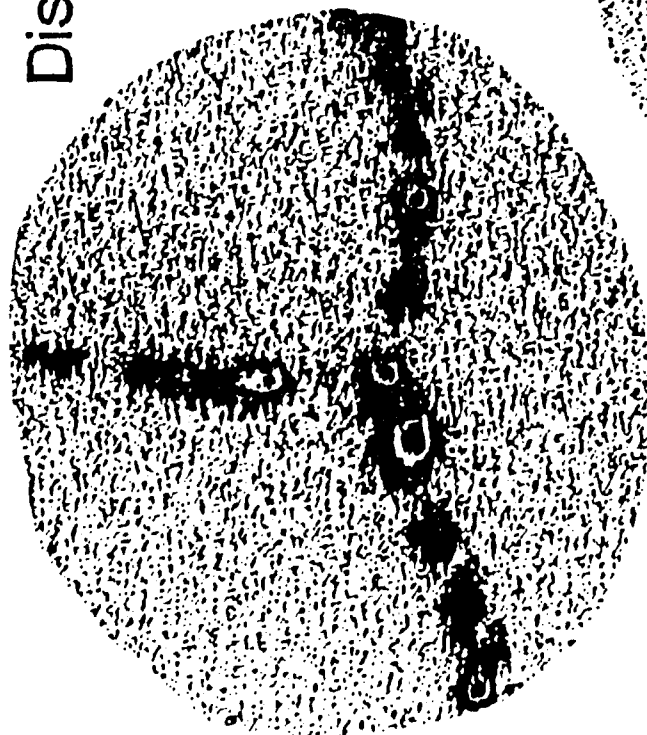


Fig. 26. Secondary ion micrographs showing gettering of Ti impurity clusters in dislocation lines in LPE-HgCdTe films

## Secondary Ion Micrographs Showing Gettering of Si Impurities on Dislocation Lines in LPE-HgCdTe Films



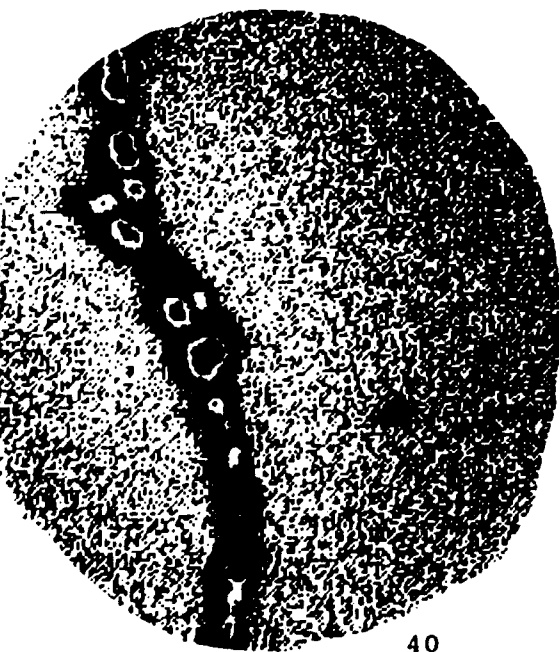
39

Fig. 27. Secondary ion micrographs showing gettering of Si impurities on dislocation lines in LPE-HgCdTe films

0127

# Secondary Ion Micrograph Plots Showing Gettering of Impurities on Dislocation Lines

M/Z 64 (TiO Features,  
Zn Background)



M/Z 30 (Si)



M/Z 54 (Fe)

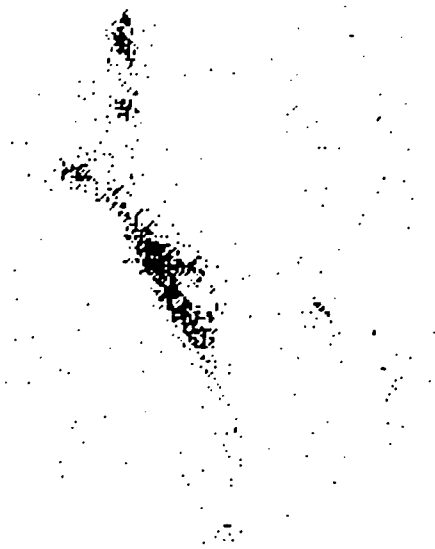


Fig. 28. Secondary ion micrographs showing getting of impurities on dislocation lines in LPE-HgCdTe films

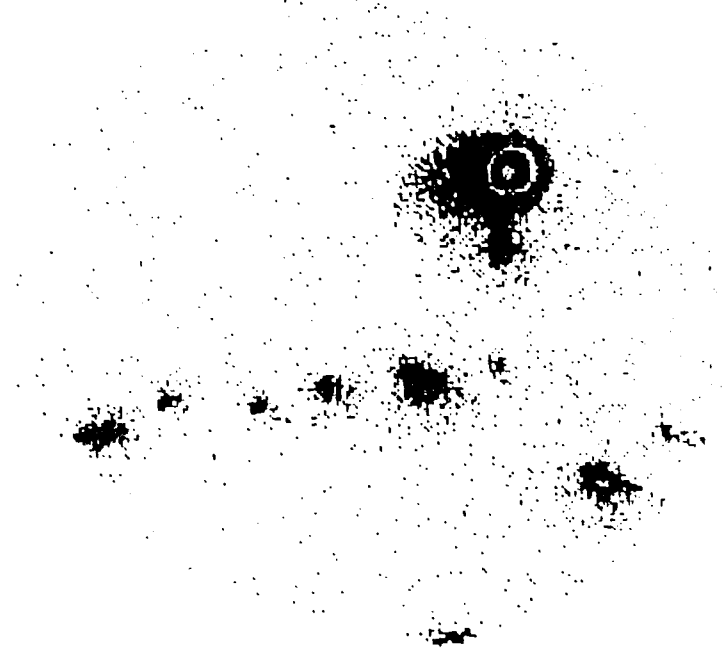
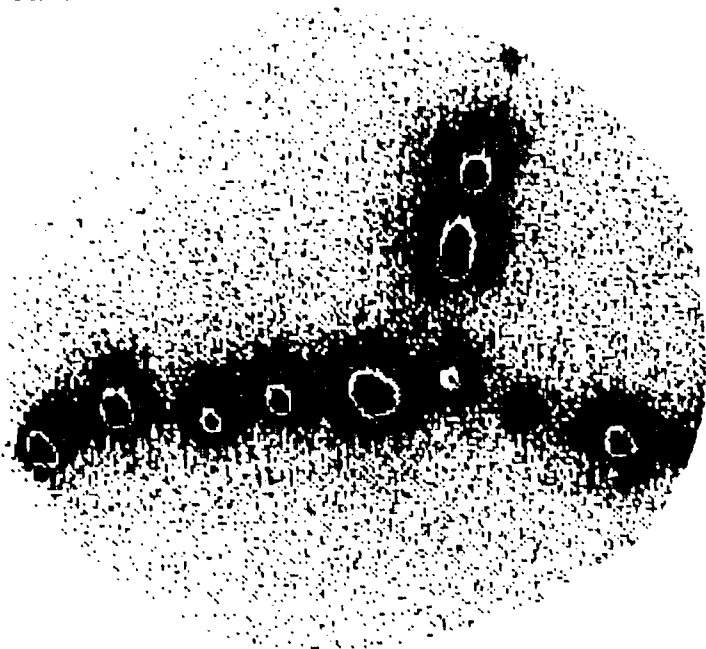
0057



# Secondary Ion Micrograph Plots Showing Gettering of Impurities on Dislocation Lines in LPE-HgCdTe Films

M/Z 48 (Ti)

M/Z 28 (Si)



M/Z 54 (Fe)

M/Z 12 (C)

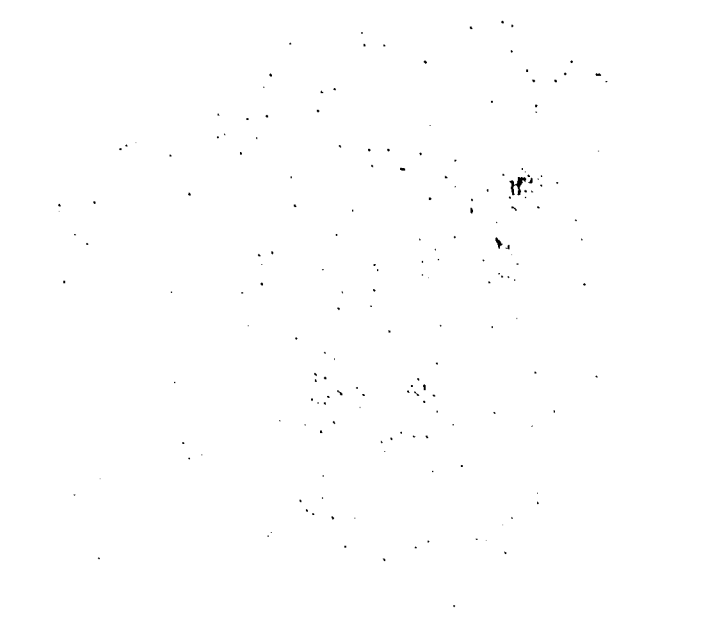
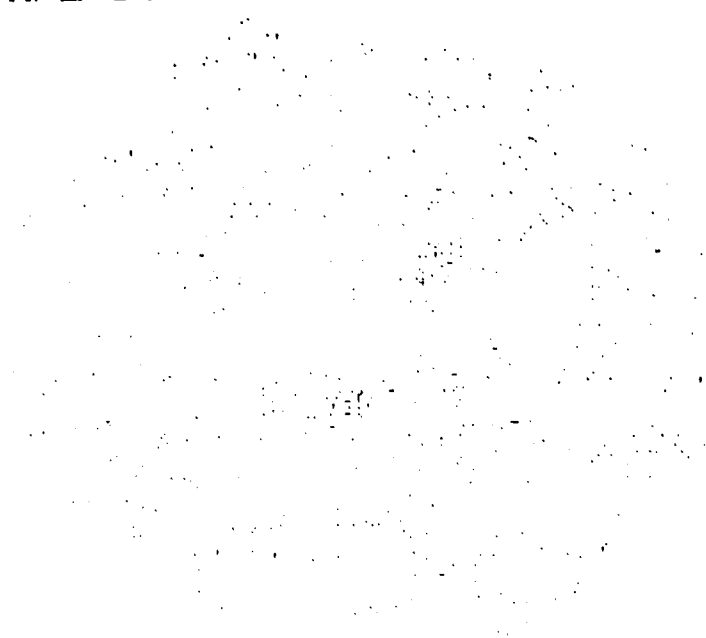
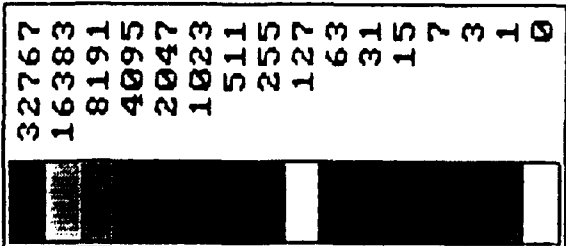
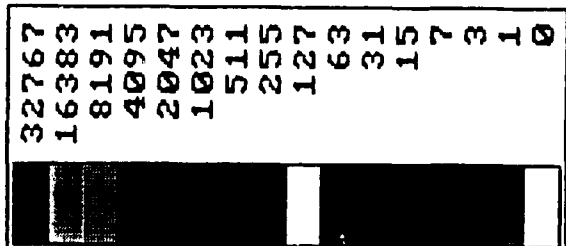


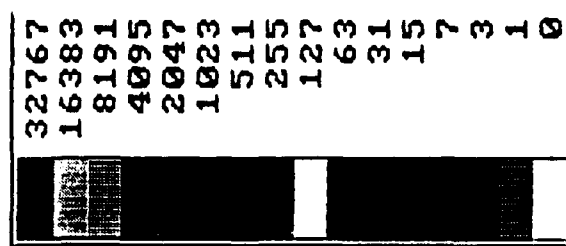
Fig. 29. Secondary ion micrographs showing gettering of impurities on dislocation lines in LPE-HgCdTe films



\RAE\  
 BRF8728D  
 2 bytes  
 Log base 2



\RAE\  
 BRF8728E  
 2 bytes  
 Log base 2



\RAE\  
 BRF8728F  
 2 bytes  
 Log base

Three Overlapping Adjacent Areas  
28Si

<--- 100 Micron --->

0059

Fig. 30. Secondary ion micrographs using digital SIMS imaging showing Si impurity clusters on dislocation lines in adjacent areas of LPE-film

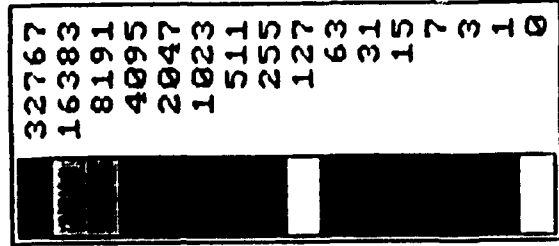
# Secondary Ion Micrographs Showing Gettering of Impurities on Dislocations in Interface Transitional Region - LPE-HgCdTe/CdTe

M/Z 30 (Si)

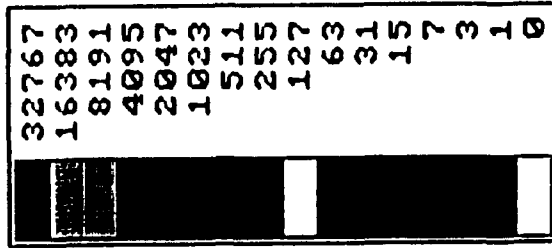
M/Z 48 (Ti)

M/Z 52 (Cr)

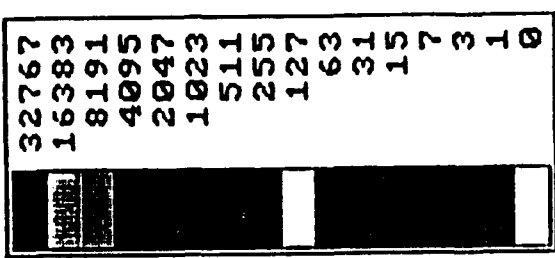
Fig. 31. Secondary ion micrographs showing getting of impurities on dislocations in interface transitional region - LPE-HgCdTe/CdTe



4  
 \RAE\  
 BRF8748F  
 2 bytes  
 Log base 2



\RAE\  
 BRF8748G  
 2 bytesM  
 Log base 2

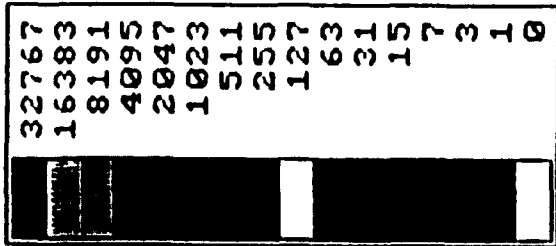


\RAE\  
 BRF8748H  
 2 bytes  
 Log base 2

Three Overlapping Adjacent Areas  
 48Ti

<--- 100 Micron --->

Fig. 32. Digital SIMS imaging of Ti impurity clusters in adjacent areas of LPE film

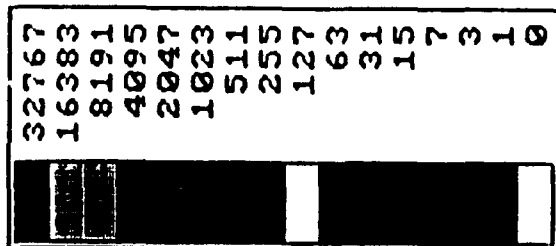


28Si

55Mn

BRF8929A  
2 bytes  
Log base 2

45

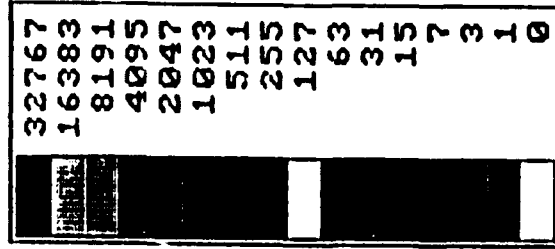


48Ti

BRF8948A  
2 bytes  
Log base 2

<--- 100 Micron --->

56Fe or 28Si2



BRF8956A  
2 bytes  
Log base 2

Fig. 33. Digital SIMS imaging showing presence of Si, Fe, Mn, and Ti clusters in selected area of LPE film

32767
16383
8191
4095
2047
1023
511
255
127
63
31
15
7
3
1
0

28Si  
 \RAE\  
 BRF9528B  
 2 bytes  
 Log base 2<sup>46</sup>

32767
16383
8191
4095
2047
1023
511
255
127
63
31
15
7
3
1
0

48Ti  
 \RAE\  
 BRF9548C  
 2 bytes  
 Log base 2

32767
16383
8191
4095
2047
1023
511
255
127
63
31
15
7
3
1
0

52Cr  
 \RAE\  
 BRF9552E  
 2 bytes  
 Log base 2

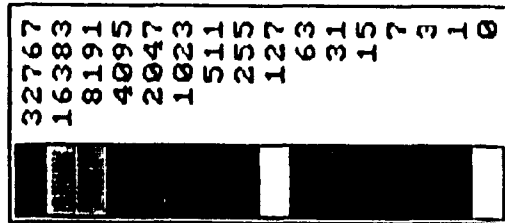
32767
16383
8191
4095
2047
1023
511
255
127
63
31
15
7
3
1
0

56Fe  
 \RAE\  
 BRF9556D  
 2 bytesM  
 Log base 2

Four Different Areas

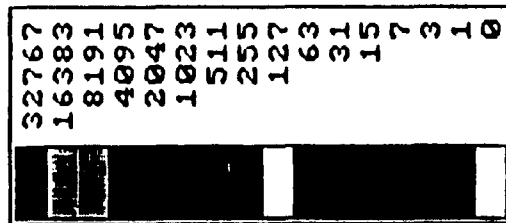
<--- 100 Micron --->

Fig. 34. Digital SIMS imaging showing presence of Si, Cr, Ti, and Fe impurity clusters in different areas of LPE film



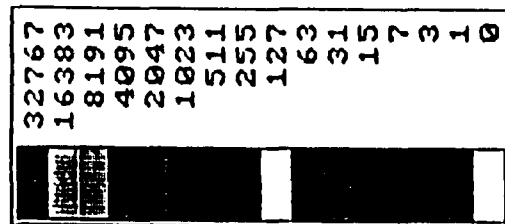
24Mg

\RAE\  
BRF9524M  
2 bytes  
Log base 2



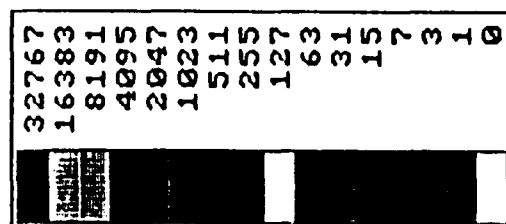
28Si

\RAE\  
BRF9528H  
2 bytes  
Log base 2



48Ti

\RAE\  
BRF9548K  
2 bytes  
Log base 2



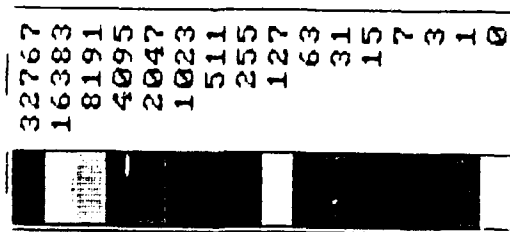
56Fe or 28Si2

\RAE\  
BRF9556J  
2 bytes  
Log base 2

Four Different Areas

<--- 100 Micron --->

Fig. 35. Digital SIMS imaging obtained slightly above transitional region (d = 3 um) of LPE film showing presence of Mg, Ti, Si, and Fe clusters



28Si

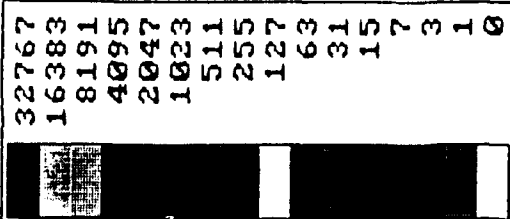
68Zn



\\RAE\\  
BRF8728A  
2 bytesM  
Log base 2

79

Four Consecutive Images, Same Area

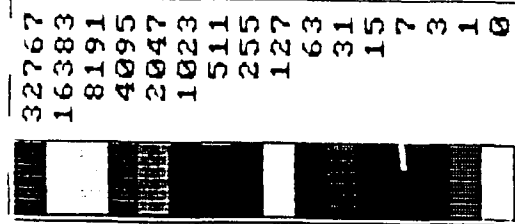


48Ti

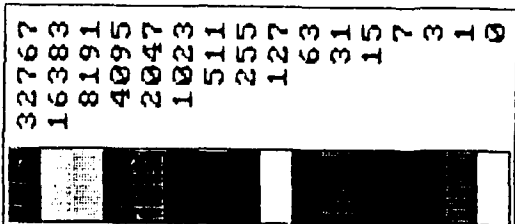
<--- 100 Micron ---> 56Fe or 28Si2



\\RAE\\  
BRF8748A  
2 bytes  
Log base 2



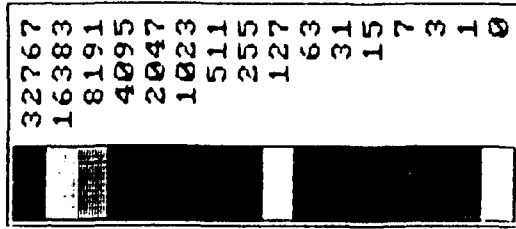
\\RAE\\  
BRF8768A  
2 bytes  
Log base 2



\\RAE\\  
BRF8756A  
2 bytes  
Log base 2

Fig. 36. Digital SIMS imaging obtained on LPI-HgCdTe/cdZnTe structure presence of Si and Ti and negligible Zn clusters

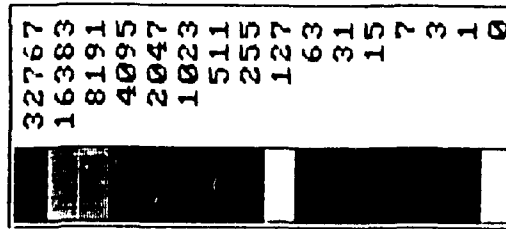




28Si

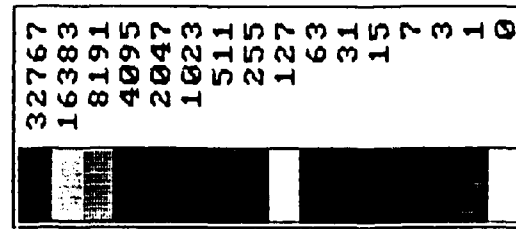
\\RAE\\  
BRF8928C  
2 bytes  
Log base 2

4



48Ti

\\RAE\\  
BRF8948C  
2 bytes  
Log base 2



56Fe or 28Si2

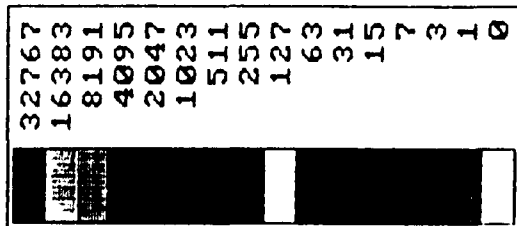
\\RAE\\  
BRF8956C  
2 bytesM  
Log base 2

Same Area For All Three Images

<--- 100 Micron --->

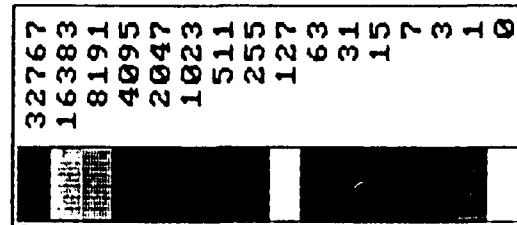
0061

Fig. 37. Digital SIMS imaging showing presence of Si, Fe, and Ti clusters in LPE film-100A



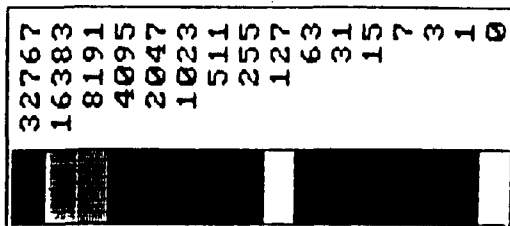
28Si

\RAE\  
BRF87281  
2 bytes  
Log base 2<sup>50</sup>



56Fe or 28Si2

\RAE\  
BRF87561  
2 bytes  
Log base 2



48Ti

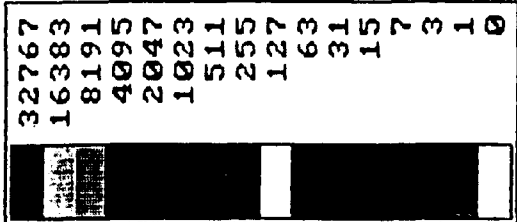
\RAE\  
BRF87481  
2 bytes  
Log base 2

Same Area For All Three Images

<--- 100 Micron --->

0062

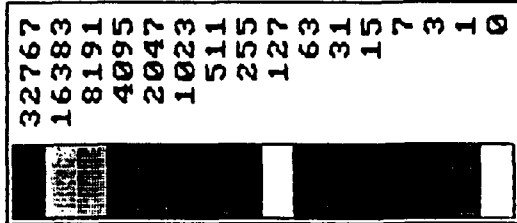
Fig. 38. Digital SIMS imaging showing presence of Si and Ti in selected area of LPE-film-100A



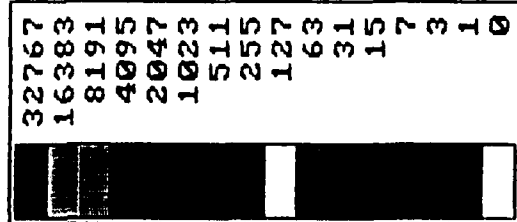
28Si

56Fe or 28Si2

RAE  
BRF8928B  
2 bytes  
Log base 2



RAE  
BRF8956B  
2 bytes  
Log base 2



48Ti

Same Area For All Three Images

<--- 100 Micron --->

RAE  
BRF8948B  
2 bytes  
Log base 2

0063

Fig. 39. Digital SIMS imaging showing presence of Si, Fe, and Ti in adjacent area (Fig. 38) of LPE-film-100A

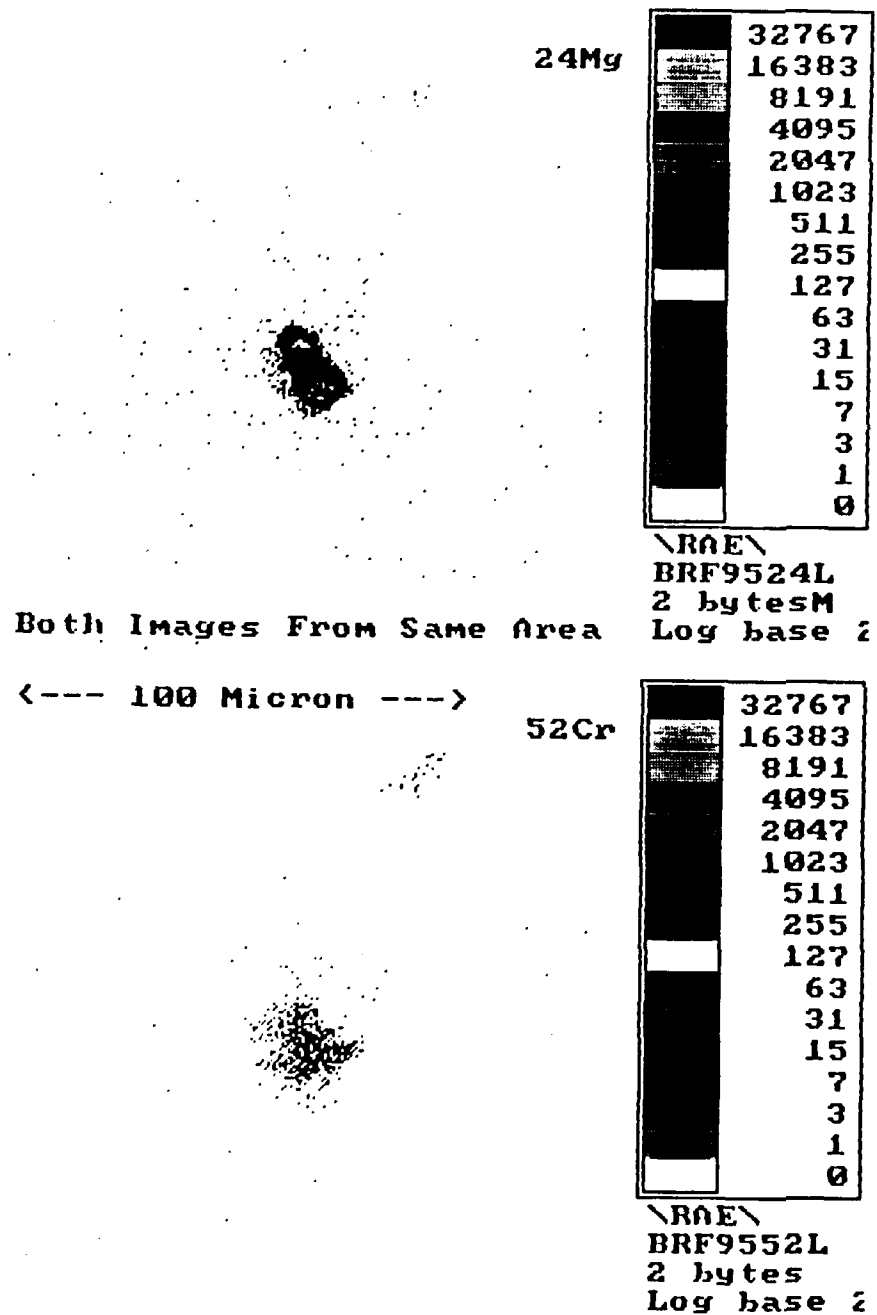
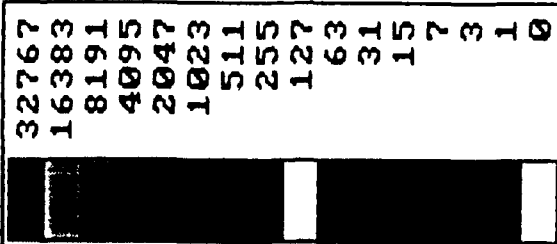
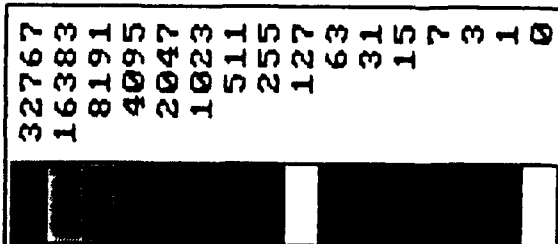


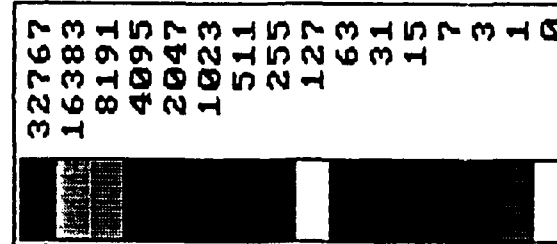
Fig. 40. Digital SIMS imaging showing presence of Mg and Cr in area of LPE-film



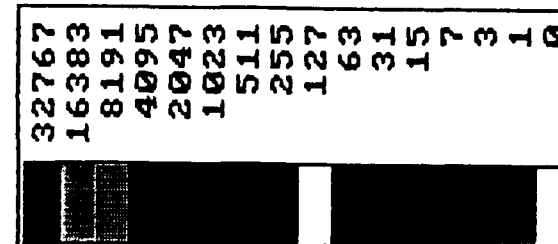
\RAE\  
 BRF9328G  
 2 bytes  
 Log base 2<sup>53</sup>



\RAE\  
 BRF9328H  
 2 bytes  
 Log base 2



\RAE\  
 BRF9328I  
 2 bytes  
 Log base 2



\RAE\  
 BRF9328K  
 2 bytes  
 Log base 2

Si From Four Different Areas

<--- 100 Micron --->

0065

Fig. 41. Digital SIMS imaging of Si impurity clusters in transitional zone of LPE-film

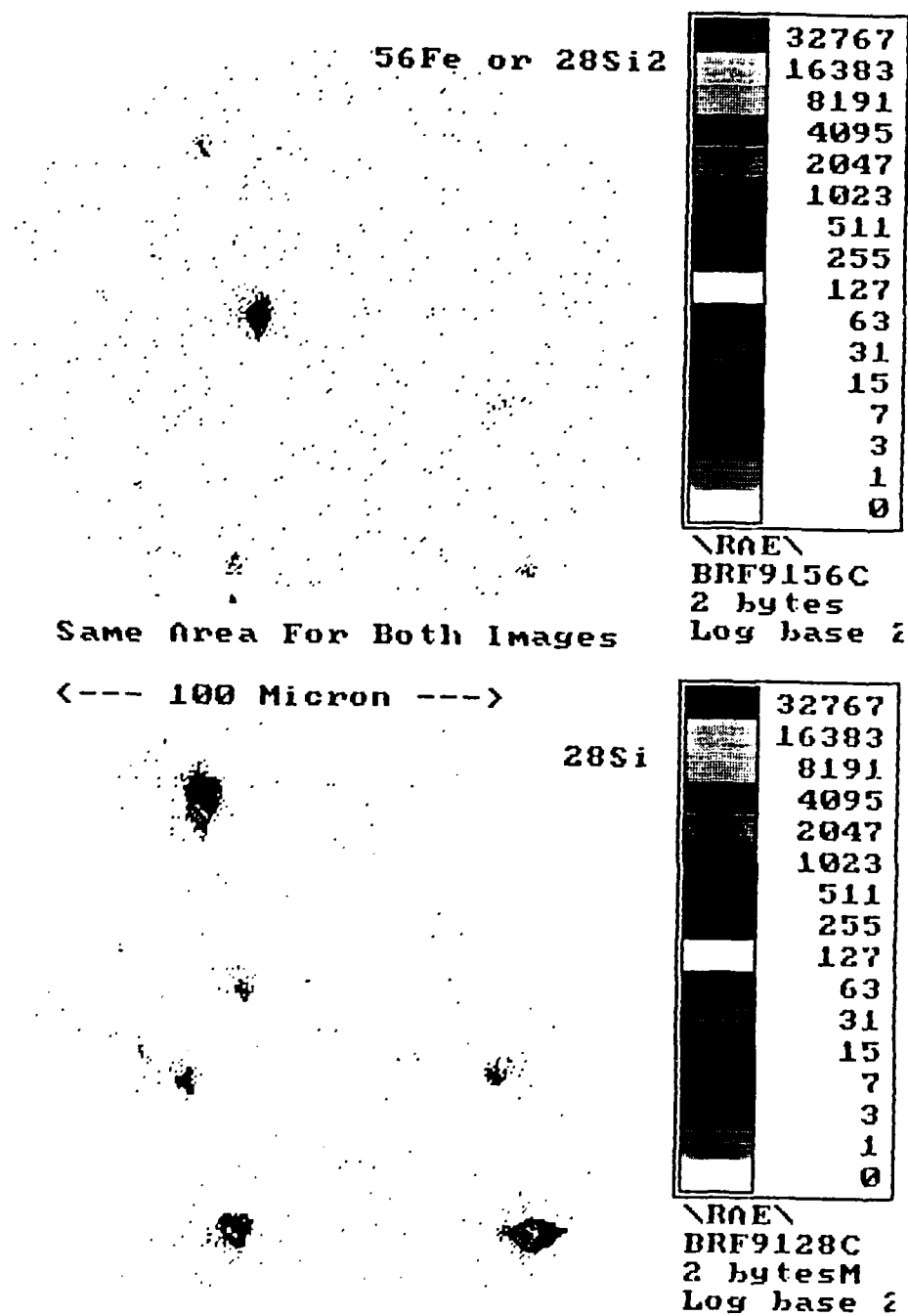


Fig. 42. Digital SIMS imaging of Si and Fe impurity clusters in LPE-film

0066

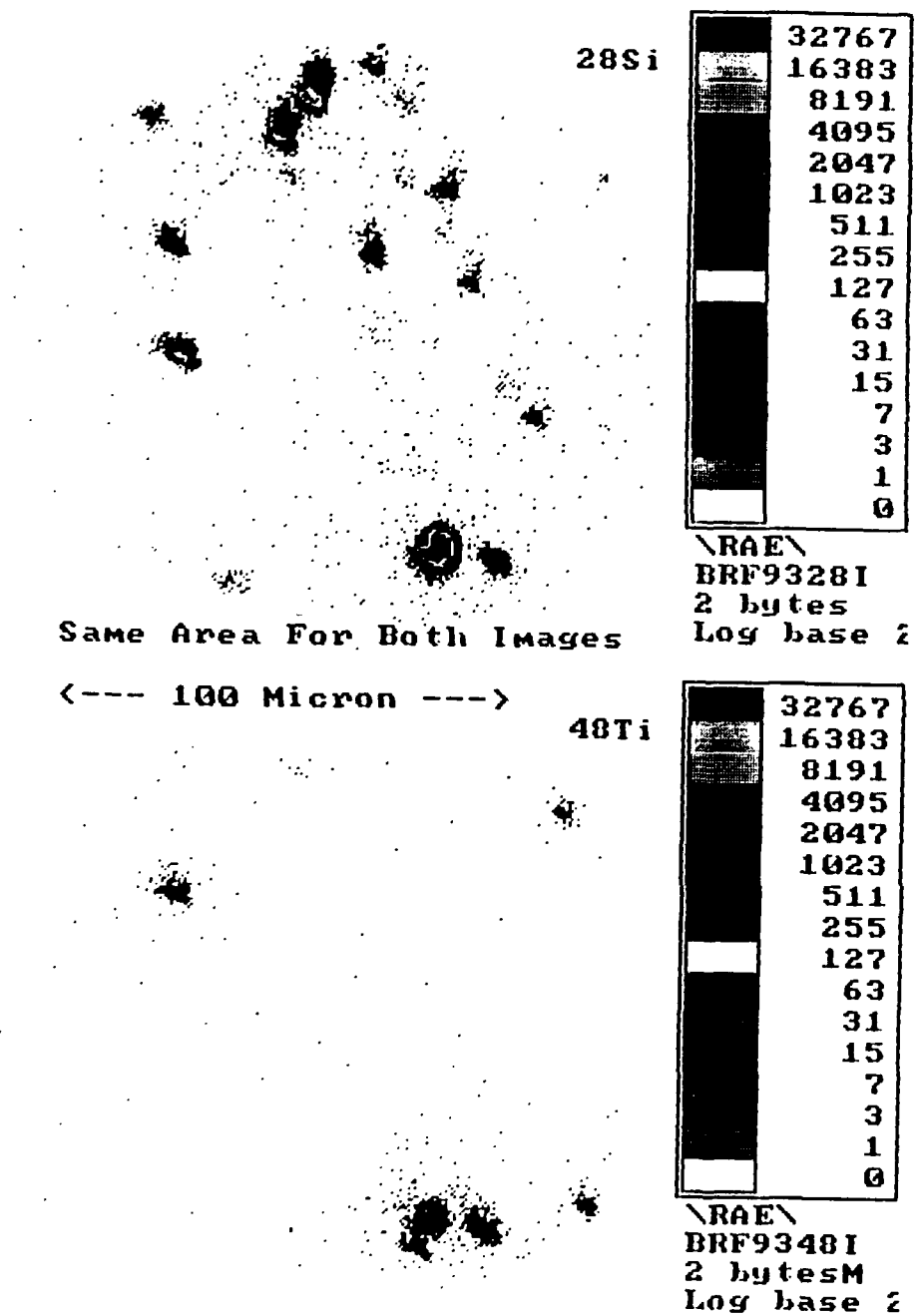
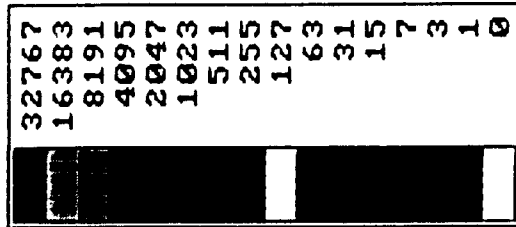
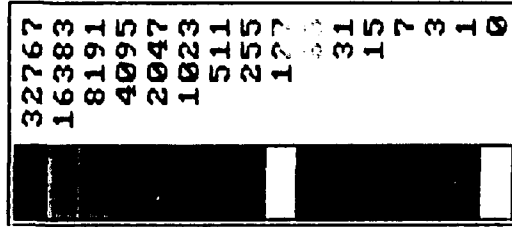


Fig. 43. Digital SIMS imaging of Si and Ti clusters in LPE-film

0067



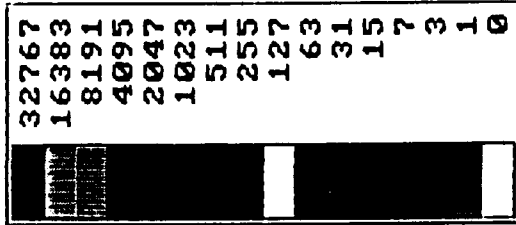
\RAE\  
 BRF8928D  
 2 bytes  
 Log base 2



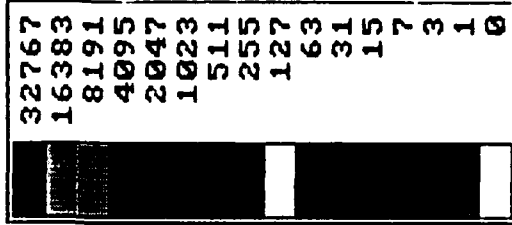
\RAE\  
 BRF8928C  
 2 bytes  
 Log base 2

Four Different Areas, 28Si

<--- 100 Micron --->



\RAE\  
 BRF9128D  
 2 bytes  
 Log base 2

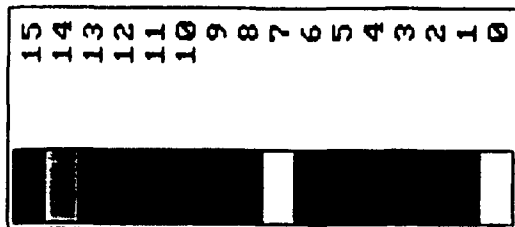


\RAE\  
 BRF9128B  
 2 bytes  
 Log base 2

0068

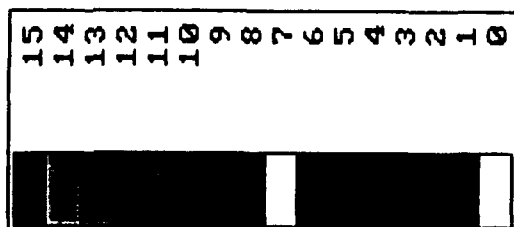
Fig. 44. Digital SIMS imaging of Si clusters in separate areas of LPE film





\RAE\  
106SFEl  
1 byte  
Linear

57



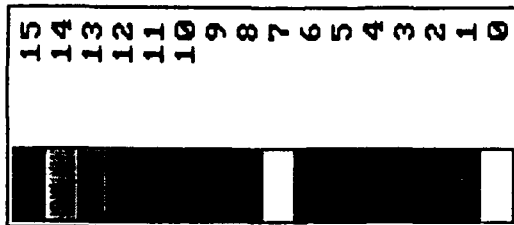
\RAE\  
106SSI1  
1 byte  
Linear



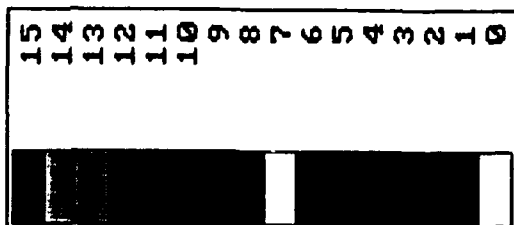
Cu image



Ti image



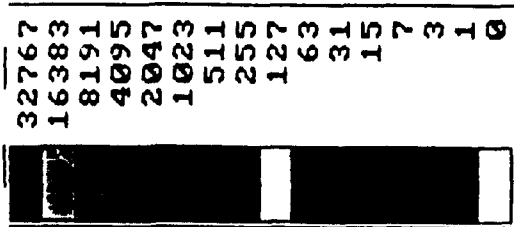
\RAE\  
106SCU1  
1 byte  
Linear



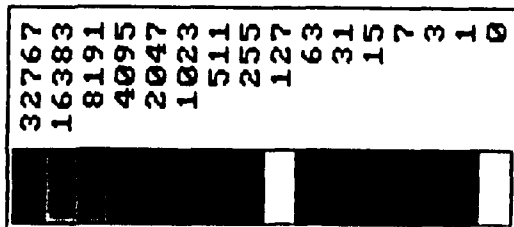
\RAE\  
106STI1  
1 byte M  
Linear

Fig. 45. Digital SIMS imaging of clusters gettered along threading dislocation lines of LPE-film

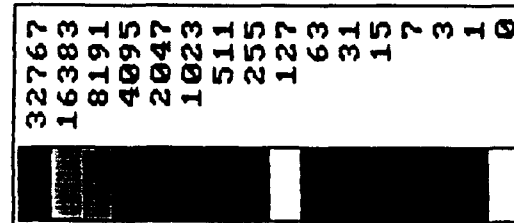
0069



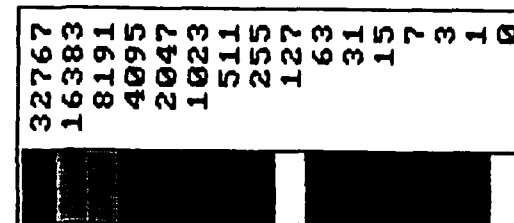
RAE  
BRF9324K  
2 bytes  
Log base 2



RAE  
BRF9327K  
2 bytes  
Log base 2



RAE  
BRF9328K  
2 bytes  
Log base 2



RAE  
BRF9356K  
2 bytes  
Log base 2

Same Area For All Four Images

<--- 100 Micron --->

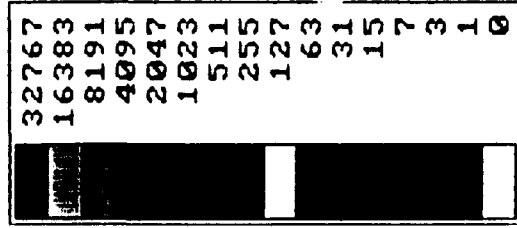
Fig. 46. Digital SIMS imaging of step-etched film (Fig. 8) showing presence of Mg and Al along substrate remnant damage traces propagating into epi-layer and Si and Fe in adjacent sites

These zones are associated with polishing induced particulates and impurities retained along remnant damage structure in the near-surface region. Of interest in the regions adjacent to lineated (decorated) remnant damage traces in the epilayer is the presence of Fe and Si clusters in discrete sites.

In MBE and MOCVD films, we observe a higher density of impurity clusters and a wider range of impurity species for the latter. In Fig. 47, we show a representative ion micrograph obtained at approximately the middle of an MBE film. Impurity clusters containing Mg, Cr, Fe, Si, Ni, and Mn are noted and obtained reproducibly from a number of films. Since these are all apparently in bound sites and hence, generally in non-radiative states, it is not surprising that conventional techniques have not been successful in detecting these impurities. It is also not surprising that double-crystal X-ray rocking curves have not detected the presence of impurity clusters. The spatial distribution and small size of the majority of these sites would effectively preclude any resolution of distributed sites.

Representative digital SIMS images obtained from MOCVD films are shown in Figs. 48 and 49. Clusters composed of Fe, Ti, Ni, Mg, Cu, Si, O, C, Zn, and Al are routinely observed in all of the MOCVD films examined. Relative to other technologies for HgCdTe deposition, the MOCVD technique produces films with the highest concentration of impurity clusters, as anticipated. Purity of precursor gases is expected to be the dominant source, although other sources also play a role in controlling the purity of MOCVD films.

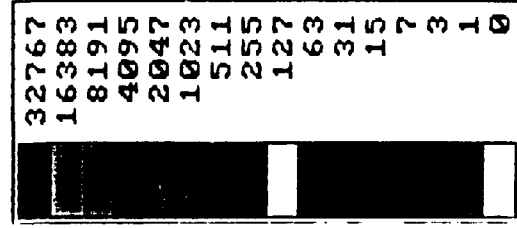
In the limited areas where visible evidence of impurity clusters (Fig. 50) could be detected in THM-HgCdTe material, we found Fe, Mg, O, and C. However, the total concentration and spatial distribution of impurity sites was dramatically reduced in comparison to other growth techniques. It is conceivable that small sites of bonded impurities may be present along dislocation lines in THM material and the detection capabilities of the current techniques do not permit adequate resolution. To address this issue, TEM studies are currently being conducted to identify any gettering or isolation within core sites along dislocation line traces.



\RAE\  
BRF9524R  
2 bytes  
Log base 2

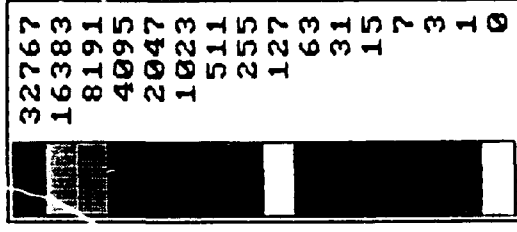
24Mg

20



\RAE\  
BRF9552R  
2 bytes  
Log base 2

52Cr



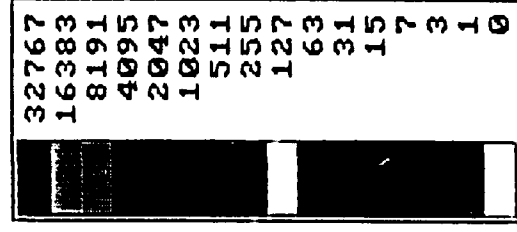
\RAE\  
BRF9556R  
2 bytes  
Log base 2

56Fe or 28Si2

Four Images From Same Area

<--- 100 Micron --->

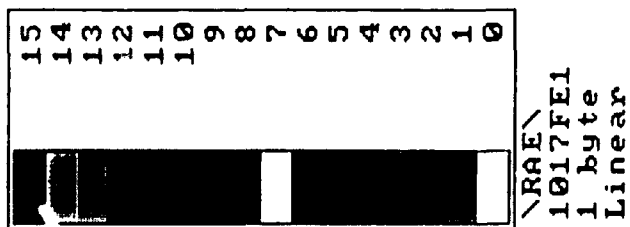
60Ni



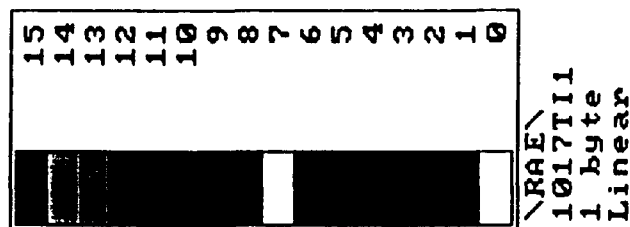
\RAE\  
BRF9560R  
2 bytes  
Log base 2

0133

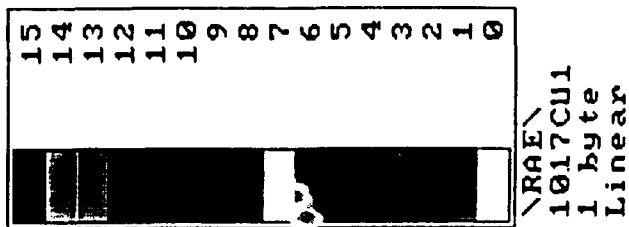
Fig. 47. Digital SIMS imaging obtained on MBE-film showing presence of Mg, Fe, Cr clusters



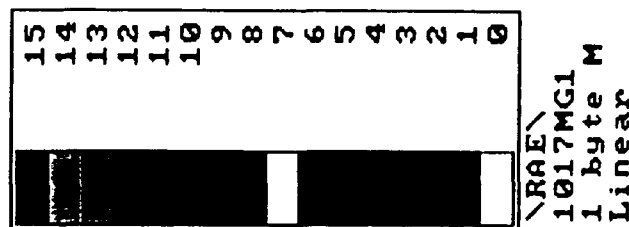
Fe image



Ti image

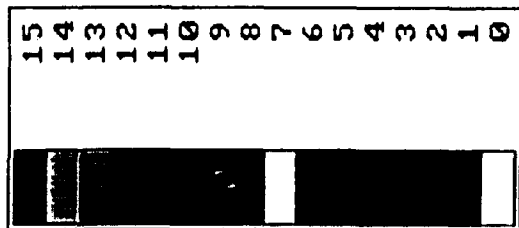


Cu image



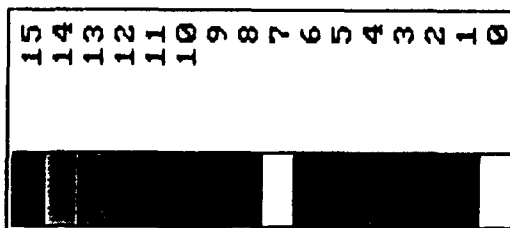
Mg image

Fig. 48. Digital SIMS imaging obtained on MOCVD-film showing presence of Mg, Fe, Cr, and Ti impurity clusters

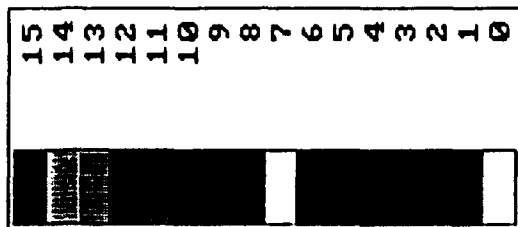


\RAE\  
1017ZN1  
1 byte  
Linear

62



\RAE\  
1017AL1  
1 byte  
Linear



\RAE\  
1017SI1  
1 byte  
Linear

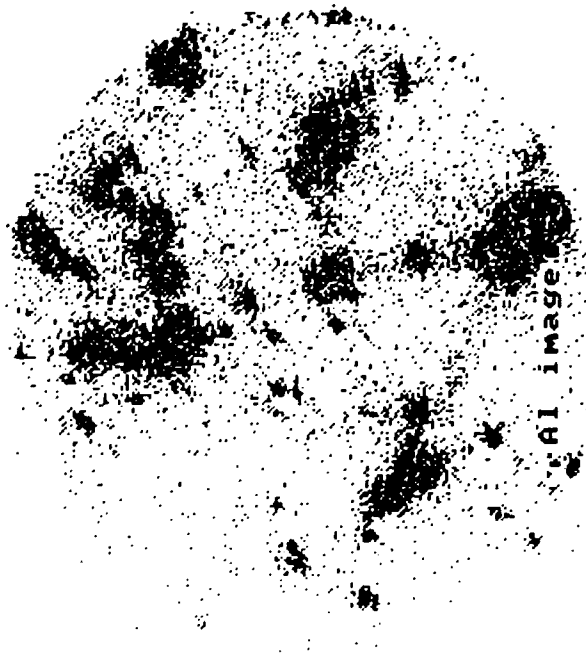


Fig. 49. Digital SIMS imaging obtained on MOCVD-film showing presence of Zn, Si, and Al impurity clusters

0071

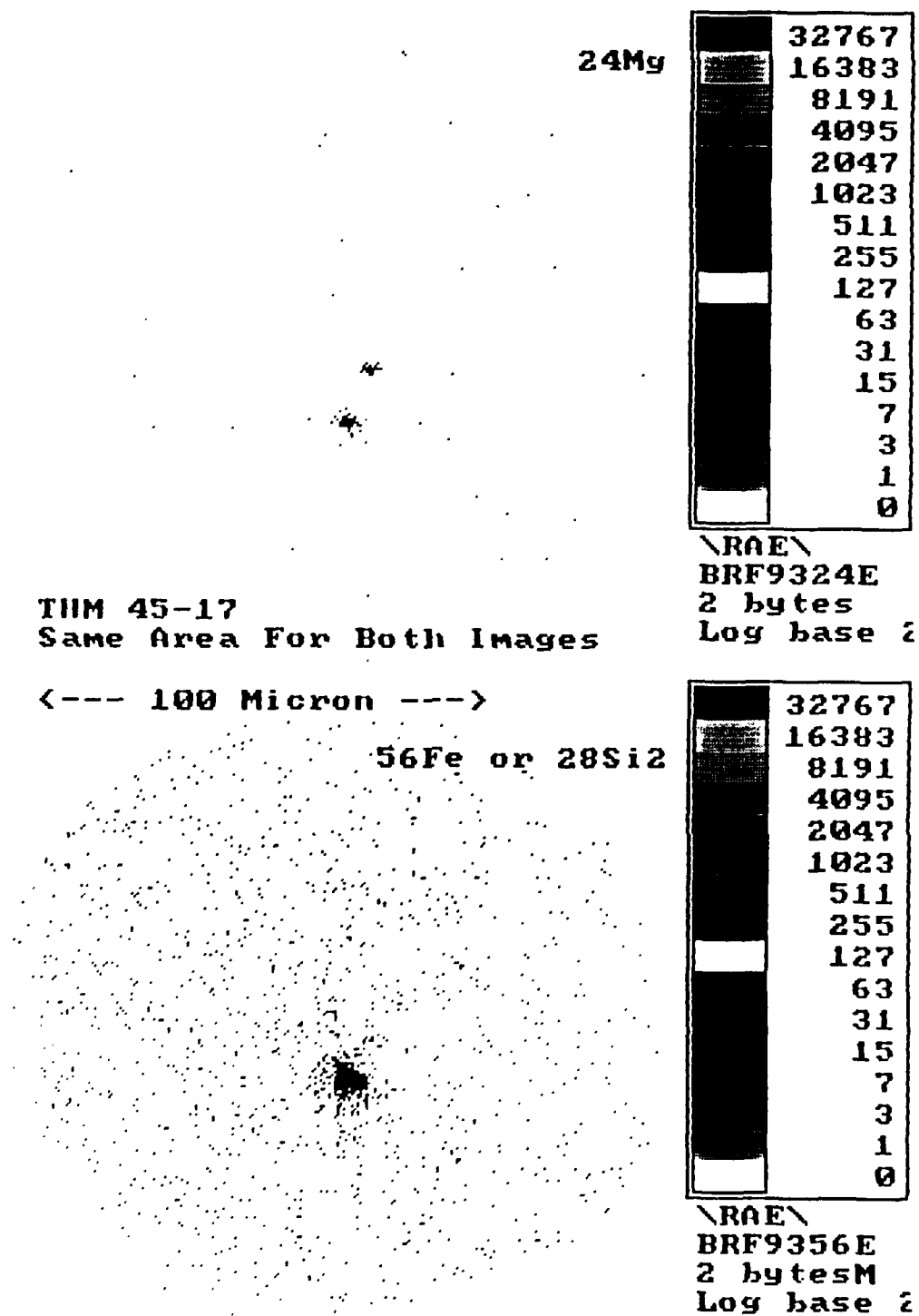


Fig. 50. Digital SIMS imaging showing presence of Mg and Fe impurity clusters in THM-HgCdTe material

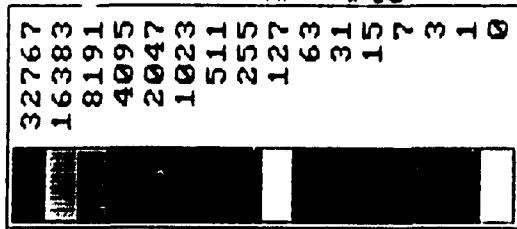
## 6.0 IMPURITY CLUSTER CORE SITES

Nucleation of impurities along dislocation lines or in discrete sites is known to be controlled by the presence of core or kernel sites in both elemental and binary semiconductors. Such nucleation sites are in the form of inert impurities, Frenkel defect assemblages, or semi-crystalline or amorphous second phase sites that may be metastable in the lattice. For Si, these sites are typically C surrounded by  $\text{SiO}_x$  precipitates. In GaAs, the sites are C surrounded by  $\text{Ga}_x\text{O}_y$ . In AlGaAs preliminary data suggests a C nucleation site with bonding to other metallics. In other ternary compounds, impurity nucleation near dislocation lines is enhanced in the presence of point defects or dislocation loops.

For HgCdTe, the question of available nucleation sites for impurities has been an area of speculation and animated gesticulation for some period of time. The existence of Te precipitates in HgCdTe has been shown by the authors in earlier studies and subsequently demonstrated by other investigators at a later date. In addition, theoretical studies by TI has been shown that retrograde solubility must be carefully considered and that Te precipitates can exist in material grown on either the Te or Hg corner, confirming experimental data reported in 1981-1982. In other studies, it has been inferred that oxygen additions to HgCdTe may control doping but reproducible data has not been reported within the industry. Alternatively, it was suggested that oxygen may nucleate, particularly in heavily defected zones, resulting in potential kernel or core sites for impurity bonding or segregation.

To investigate core sites in more detail, we probed impurity cluster sites for excess Te within the local region. In Fig. 51 within the central region of the field, we show a high concentration of Si and Ti. Also, clearly shown in this zone is the presence of excess Te, essentially identifying the core site. Within this same field, we also detect other core sites of Te within impurity zones, although less well-defined than the center site. Examination of other samples also shows small Te core regions that duplicate this result. The nature of bonding is at present unidentified, but will be explored in more detail in ongoing studies.



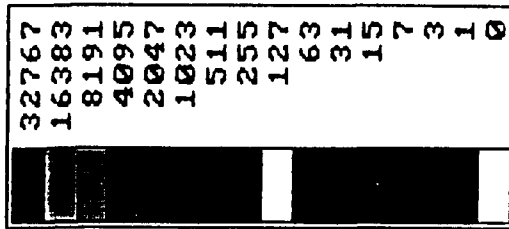


M/Z 30 (Si)

\RAE\  
BRF5730D  
2 bytes  
Log base 2

65

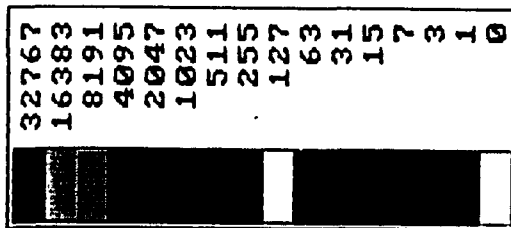
HgCdTe  
8-04-59



M/Z 48 (Ti)

\RAE\  
BRF5748F  
2 bytesM  
Log base 2

M/Z 122 (Te)



\RAE\  
BRF57122  
2 bytes  
Log base 2

Fig. 51. Clustering in 48-hour 270°C annealed HgCdTe showing high concentration of Si and presence of Te core in central precipitate

0073

The presence of O and C is often detected in LPE films, although more dominantly in MOCVD layers. Insufficient data exists at this time to definitively isolate O or C as a core site in LPE structures. However, due to the high concentration of both O and C introduced in the precursors for MOCVD layer growth, nucleation areas are more prevalent and can be investigated in greater detail. In Fig. 52, we show that oxygen and carbon are found as associates and that impurities are also nucleated on these sites. The nature of bonding or reaction is unknown, but the observation of impurity associates on O/C sites is routinely observed.

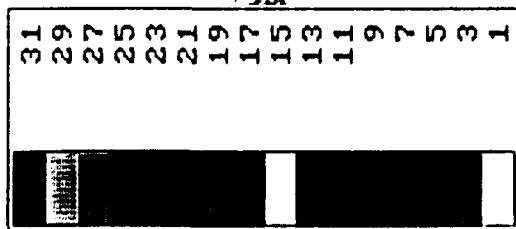
#### 7.0 NON-EQUILIBRIUM THERMODYNAMIC CONSIDERATIONS OF IMPURITY DIFFUSION DURING GROWTH<sup>4</sup>

The observation of localized segregation of impurities in strained or defect regions of HgCdTe must be considered in terms of a non-equilibrium process during growth. Segregation or localization of impurities will be controlled by spatial fluctuations in the growth process as well as other external perturbations in the impurity - HgCdTe matrix system. Structural and dynamic effects are closely related, i.e., equilibrium is maintained by rapid molecular motion and interaction. Even though macroscopic parameters are time-independent in equilibrium, the values are maintained by time-dependent processes. These include: thermal gradients, dislocation line generation and climb, strain gradients, enhanced local diffusion and changes in potential introduced by inert sites, among others.

To obtain a stochastic description of impurity diffusion and segregation, one must introduce an ensemble. To describe the dynamic process, an ensemble can be constructed such that each system contains one impurity in the melt. The position of the impurity at time,  $t = 0$ , is called  $x_0$  and the temperature is held fixed. Thus, each system is macroscopically identical but microscopically different.

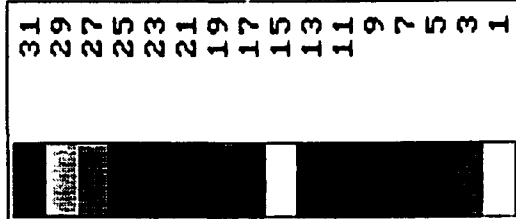
After a lapse of time, the impurities move to new positions and there is a change in microscopic parameters. If one now allows the ensemble to contain a large number of members, it is possible to construct a "conditional probability" function given by:

$$P_2(x_0 | x_t) dx \quad (7)$$



RAE/  
10170  
1 byte  
Linear

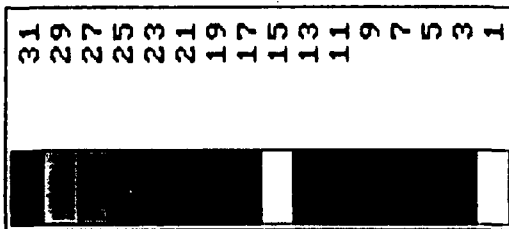
O image



RAE/  
1017SI  
1 byte M  
Linear

Si image

67



RAE/  
1017C  
1 byte  
Linear

C image

Fig. 52. Digital SIMS images obtained on MOCVD-film showing presence of Si and C and O as potential core sites

0074

where  $P_2(\underline{x}_0|\underline{x}_t)d\underline{x}$  = probability of finding impurities in a randomly chosen member of the ensemble in the position range  $\underline{x}$  to  $\underline{x} + d\underline{x}$  at time  $t$ , if the impurities are at  $\underline{x}_0$ , at  $t = 0$ .

In terms of the ensemble

$$P_2(\underline{x}_0|\underline{x}_t)d\underline{x} = n_t(\underline{x}, \underline{x} + d\underline{x})/N \quad (8)$$

where

$N$  = number of members in the ensemble

$n_t(\underline{x} + d\underline{x})$  = number of members in the ensemble within the range,  $\underline{x}$  to  $\underline{x} + d\underline{x}$  at time,  $t$ .

For  $t \gg 0$ , this ensemble becomes an equilibrium ensemble, so that:

$$\lim_{t \rightarrow \infty} n_t(\underline{x}, \underline{x} + d\underline{x}) = n_{eq}(\underline{x}, \underline{x} + d\underline{x}) \quad (9)$$

In this case, all knowledge of the dynamical processes are lost and motion of impurities during the growth process under fixed or time-dependent fields and segregation of impurities in the crystal are not adequately described by equilibrium or steady state equations.

Impurity diffusion can be described by Fick's first law:

$$\underline{j} = -D \nabla n \quad (10)$$

where

$\underline{j}$  = the flux of impurities,  $n$  is the density of atoms,  $D$ , the diffusion coefficient, and  $\nabla$  the gradient operator.

In the presence of an external field,  $F(x)$ , a spherical impurity attains a constant velocity,  $\tilde{v}$ , defined by Stokes Law:

$$\tilde{v} = F \xi^{-1} \quad (11)$$

where  $\xi = 6\pi\eta R$   $\xi$  = the friction coefficient,  $R$ , the "radius" of the impurity and  $\eta$  is the viscosity term.

The flux of impurities associated with this velocity is:

$$\tilde{j}' = n \tilde{v} = n \xi^{-1} F \quad (12)$$

At equilibrium, there is no net flux and

$$\tilde{j} + \tilde{j}' = 0 = -D \nabla n + n \xi^{-1} F \quad (13)$$

such that:

$$\tilde{F} = \frac{\xi D}{n} \nabla n(x) \quad (14)$$

which expresses the dynamical condition of equilibrium.

The structural part of the equilibrium is defined by the chemical potential of the impurity. Since the impurities are independent, the potential is given by:

$$\mu_1 = \mu_1^0 + \phi(x) + kT \ln n(x) \quad (15)$$

where

$\phi(x)$  = the potential energy in the presence of an external field and  $\mu_1^0$  depends only on temperature.

at equilibrium,  $\delta\mu_1=0$ , such that:

$$-\nabla \phi(x) = \tilde{F} = \frac{kT}{n} \nabla n(x) \quad (16)$$

and

$$\frac{D}{kT} = \xi^{-1} \text{ (Einstein-Stokes relationship).}$$

This relationship defines the condition for equilibrium by relating a response coefficient to a transport coefficient.

In the growth of HgCdTe, solid state equilibrium equations are invalid for describing diffusion and segregation of impurities. A general description can be derived by considering the non-equilibrium probability distribution. The density of impurities at  $\underline{x}$  and time,  $t$ , is given by:

$$n(\underline{x}_0 | \underline{x}_t) = NP_2(\underline{x}_0 | \underline{x}_t) \quad (17)$$

An equation for the change in density can be obtained by assuming that the density at time,  $t + \tau$  is determined in an analogous way to the density at time,  $t$ :

$$n(\underline{x}_0 | \underline{x}_{t+\tau}) = \int n(\underline{x}_0 | \underline{y}_t) P_2(\underline{y} | \underline{x}_\tau) d\mathbf{y} \quad (18)$$

during growth and solidification:

$$P_2(\underline{y} | \underline{x}_t) = \phi(\underline{\Delta}, t) \quad (19)$$

where  $\underline{\Delta} = |\underline{y} - \underline{x}|$

Similarly, the density will depend on the radial distance from  $\underline{x}_0$ , such that:

$$n(\underline{x}_0 | \underline{x}_{t+\tau}) = n(r, t + \tau) \quad (20)$$

where  $r = |\underline{x} - \underline{x}_0|$

Therefore, the time evolution for the density as a function of  $r$  becomes:

$$n(r, t + \tau) = \int n(|\underline{\Delta} - \underline{r}|, t) \phi(\underline{\Delta}, \tau) d\underline{\Delta} \quad (21)$$

For short time intervals:

$$n(r, t + \tau) = n(r, t) + \tau \frac{\delta n}{\delta t} + \dots \quad (22)$$

The density in the integrand is expanded around  $r$  on the assumption that in a short interval,  $\tau$ ,  $\phi(\Delta, \tau)$  is appreciable only for  $\Delta \rightarrow 0$ . Thus,

$$n(|\underline{r}-\underline{r}'|, t) = n(r, t) + \nabla n \cdot \underline{\Delta} + \frac{1}{2} \underline{\Delta} \cdot \frac{\delta^2 n}{\delta r^2} \underline{\Delta} + \dots (23)$$

$$\tau \frac{\delta n}{\delta t} = \frac{1}{2} \int \underline{\Delta} \frac{\delta^2 n}{\delta r^2} \cdot \underline{\Delta} \phi(\Delta, \tau) d\underline{\Delta} \quad (24)$$

where:  $\int \phi(\Delta, \tau) d\Delta = 1$  for normalization

and  $\int \underline{\Delta} \phi(\Delta, \tau) d\underline{\Delta} = 0$  for "smoothing"

In similar fashion:

$$\int \Delta_i \Delta_j \phi(\Delta, \tau) d\underline{\Delta} = 0 \quad \text{for } i \neq j \quad (25)$$

and

$$\int \Delta_i^2 \phi(\Delta, \tau) d\underline{\Delta} = \frac{1}{3} \int \Delta^2 \phi(\Delta, \tau) d\underline{\Delta} \quad (26)$$

for an isotropic case.

From the earlier equations, we can derive:

$$\frac{\delta n}{\delta t} = K \nabla^2 n \quad (27)$$

where the non-equilibrium diffusion coefficient,  $K$ , is given by:

$$K = \lim_{\tau \rightarrow 0} \left( \int \Delta^2 \phi(\Delta, \tau) d\underline{\Delta} / 6\tau \right) \quad (28)$$

The previous equation assumes the form of Fick's second law for solid state diffusion:

$$\frac{\delta n}{\delta t} = D \nabla^2 n \quad (29)$$

However, for this case, equation 29 is valid only if  $D$  is independent of spatial coordinates and, in general, independent of  $n$ .

The general derivations presented serve to illustrate the point that impurities are distributed in regions during growth under non-equilibrium conditions and may indeed localize at that time. Subsequent annealing will move impurities into nucleation sites or near dislocations. Long diffusion distances are generally not required, since impurities are already localized in distributed zones in strained regions of the crystal during growth.

This is consistent with the random experimental observations of others on local distributions of impurities in HgCdTe and the observed clustering of metallics reported here for all available HgCdTe material. These high concentration spatially localized regions of segregated impurities are not explainable on the basis of equilibrium, spatially invariant segregation coefficients, but rather on diffusion and segregation under non-equilibrium conditions.

#### 8.0 CHARGE STATES AT THE CdTe (HgCdTe) SURFACE IN THE PRESENCE OF RESIDUAL SUBSURFACE DAMAGE AND BURIED IMPURITY CLUSTERS

Although a considerable amount of effort has been expended in improving the surface finish of CdTe (CdZnTe) and HgCdTe surfaces, residual damage remains in sporadic regions of many available substrates. Such damage not only influences the quality of epitaxial layers grown on substrates but has an effect on surface impurity adsorption and particulate adhesion.

Buried damage in the near-surface region of an insulator or semi-insulator in the form of spherical or cylindrical voids or inclusions will develop an internal charge at the outer surface area of the defect. For charge compensation, a space charge region of radius,  $r$ , will then be formed surrounding the defect. The size of the space charge zone will be dependent on the dielectric constant and strain field surrounding the defect. For subsurface damage typically observed in materials, the space charge region will overlap the physical surface, producing an "image charge" defining the geometric projection of the defect onto the surface.

To reveal the presence of such spatially defined charge, it is necessary to use a decorating charged particle that will adhere to the regions of excess charge via an electrostatic interaction. Since the charge per unit surface area on the particle is critical, as well as the size of the decorating particle, it is essential to select both the suspension



medium and the particle size distribution. To achieve this, we used a carbon particle distribution (Rayleigh) with an average size of 1400 Angstroms, suspended in a medium to induce charge on the carbon particle surfaces. The finer particles are then attracted and tightly bound to the surface charge sites. Excess particles are swept away with a deionized water rinse and the "decorated" surface examined in the optical microscope (Nomarski mode) or SEM.

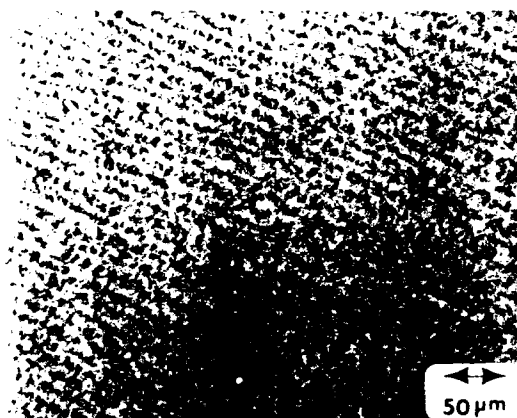
In Figs. 53 and 54 are shown sapphire and  $\text{LiNbO}_3$  surfaces after decoration. The presence of lineated buried damage and spherical defects are clearly revealed. Of interest is the fact that depth gradients of damage or traces of multiple polishing steps can be revealed, depending solely on the physical dimensions of the defect and depth below the surface. The location, distribution and nature of such structure in  $\text{Al}_2\text{O}_3$  and  $\text{LiNbO}_3$  has been analyzed in great detail using correlated data from RBS, ellipsometry and TEM obtained by the authors on earlier DoD programs.

For GaAs, Si, CdTe, and HgCdTe, similar procedures can be used to localize or delineate charge sites on surfaces. In Fig. 55 is shown a decorated GaAs surface showing the presence of both subsurface damage and buried clusters. This type of lineation is seen on all GaAs wafers and has been correlated with an extensive amount of destructive and nondestructive analytical data over the past four years.

Figure 56 shows a commercially available (as received) CdTe wafer decorated to reveal the presence of subsurface damage and buried impurity clusters. This type of lineation is seen to varying degree on many CdTe substrates. Improved surface finish shows only sporadic "pockets" of buried damage and distributed charged site lineation caused by the presence of bulk impurity clusters near the surface region.

The critical point to be made is that surface charge is inevitably present on II-VI material surfaces attributable either to residual damage or buried impurity clusters. On "razor-blade" cleaved HgCdTe surfaces, we also observe similar lineated structure caused by deformational spikes introduced possibly by an acoustic wave or irregular travel of the blade.

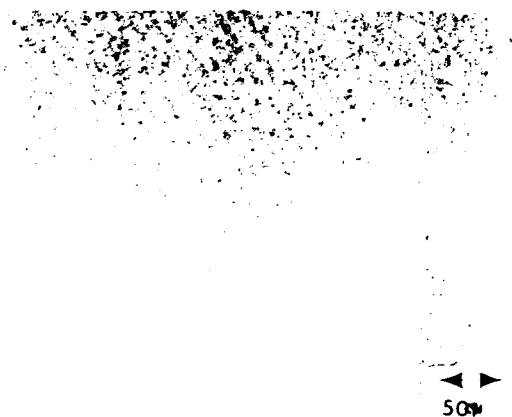
## RESIDUAL SURFACE DAMAGE SAPPHIRE SUBSTRATES(DECORATED)



HIGH DEFECT DENSITY REGION



MODERATE, SCATTERED DEFECTS



MODERATE DEFECT DENSITY  
REGION



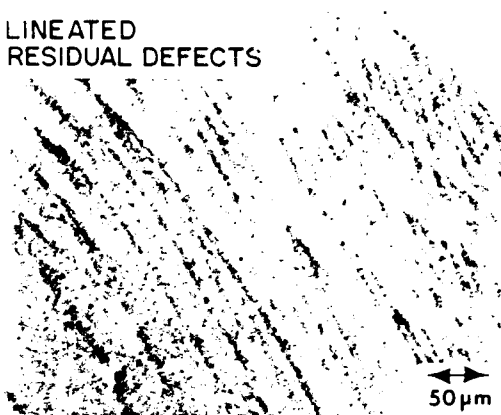
LOW DEFECT DENSITY REGION

Fig. 13. Optical micrographs (Nomarski mode) obtained on sapphire surfaces after decoration showing presence of extensive buried (charged) lineated damage traces (Ref. 1)

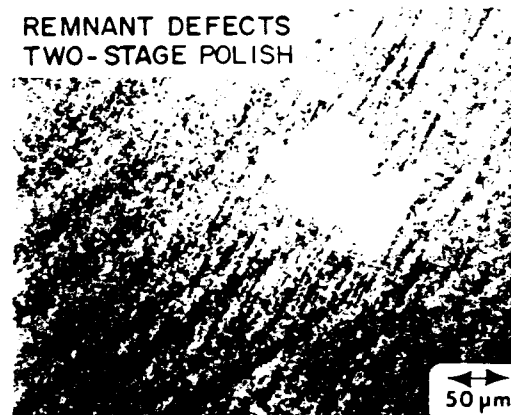
0075

# CONVENTIONALLY POLISHED LiNbO<sub>3</sub> SURFACES (DECORATED)

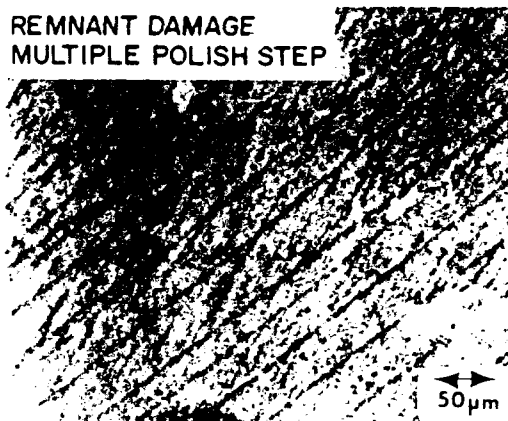
LINEATED  
RESIDUAL DEFECTS



REMNANT DEFECTS  
TWO-STAGE POLISH



REMNANT DAMAGE  
MULTIPLE POLISH STEP



LINEATED  
DEFECT TRACES

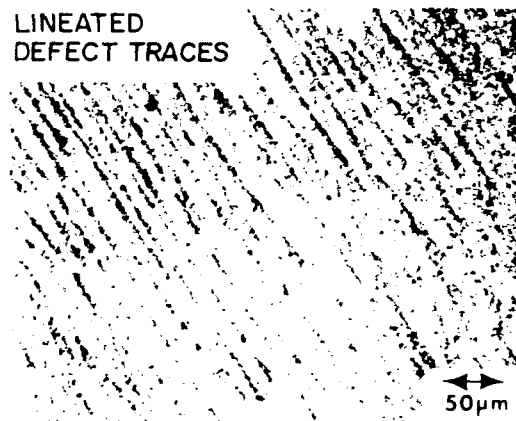


Fig. 1. Optical micrographs (Nomarski mode) obtained on lithium niobate surfaces after decoration showing presence of extensive buried (charged) lineated damage at varying depths associated with multiple polishing steps. (Ref. 1)

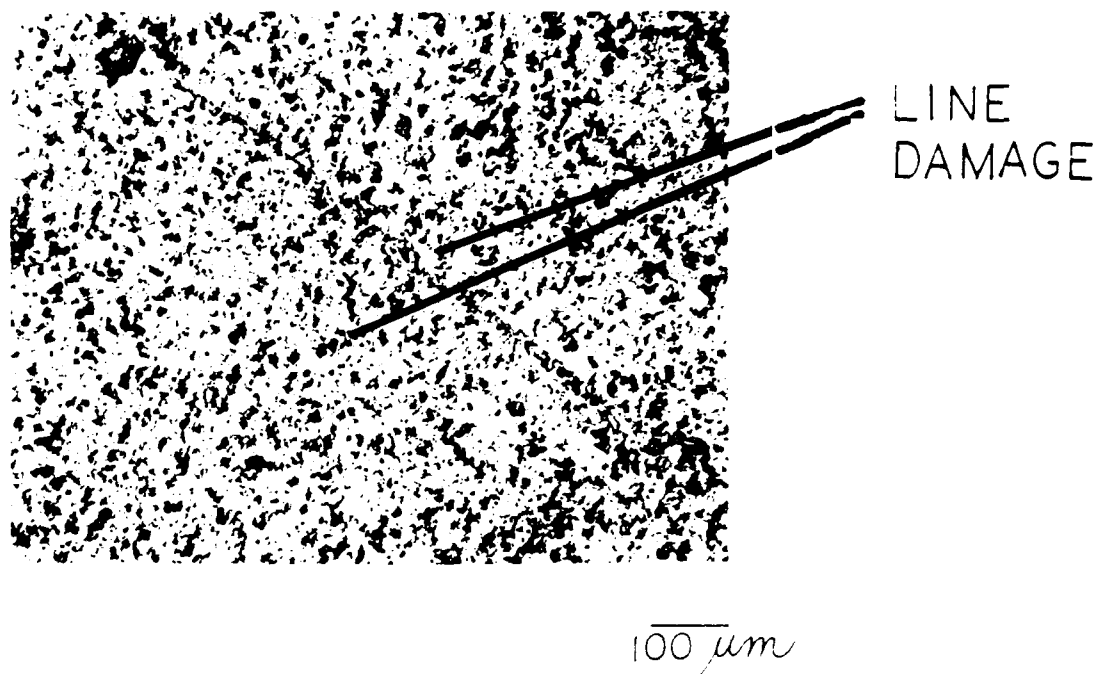


Fig. 55. Optical micrographs (Nomarski mode) of decorated surfaces showing charged states associated with buried damage and clusters (Ref. 1)

0077

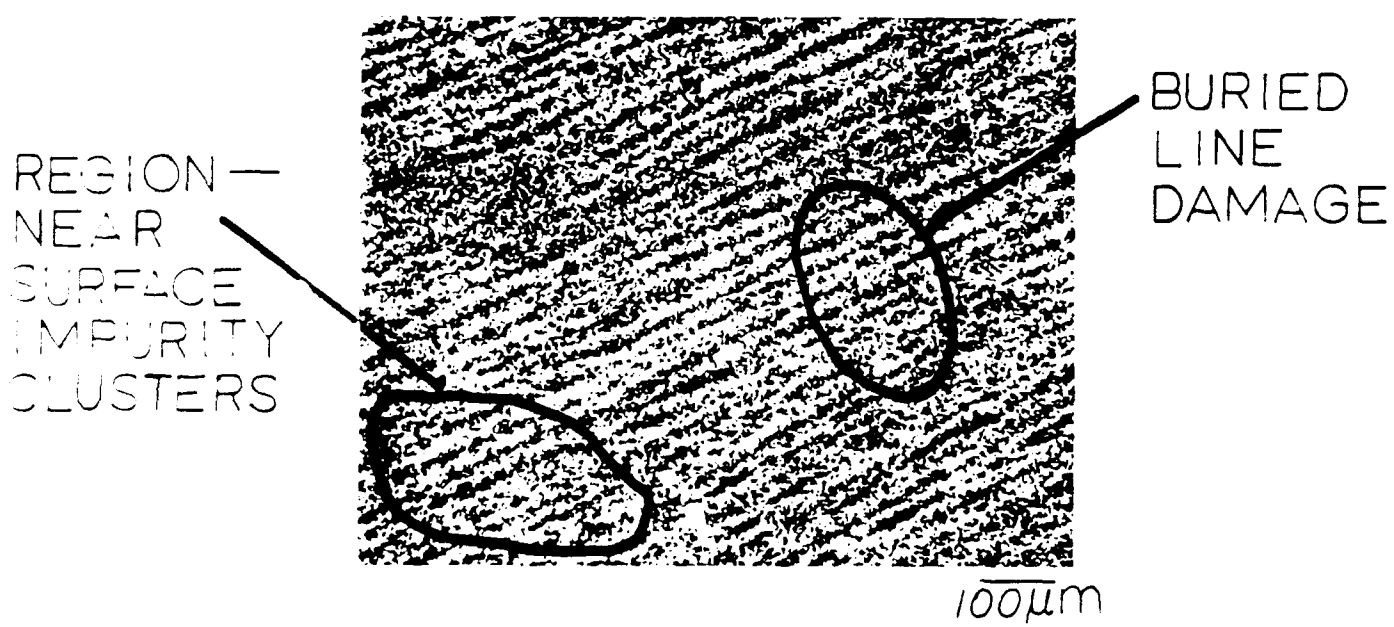
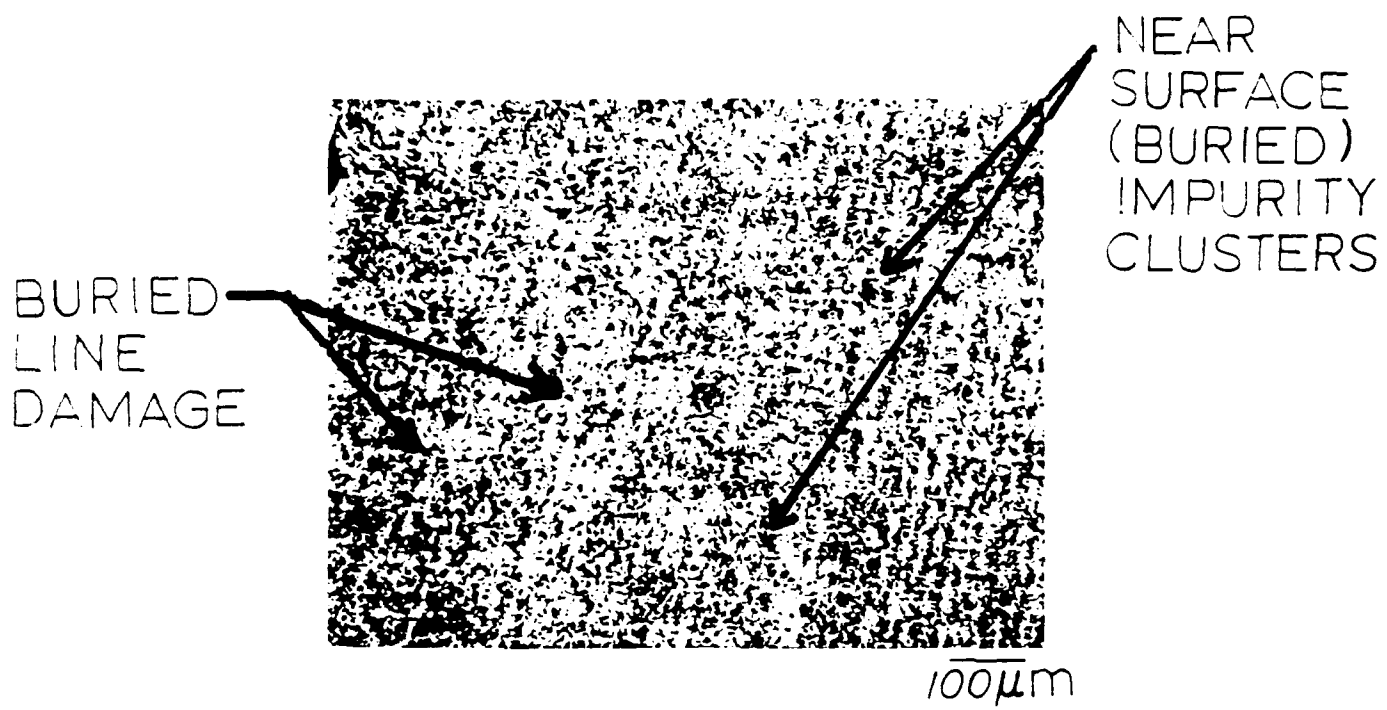


Fig. 56. Optical micrograph of decorated CdTe surface showing presence of charge states associated with presence of buried remnant damage and impurities

The presence of the defect induced surface charge has also been shown to produce local alterations in oxidation, increases in particulate/impurity attraction and may explain some of the anomalies reported for MIS structures. However, the MIS structures are additionally complicated by the presence of impurity spiking at the interface introduced during anodization or plasma deposition.

#### 9.0 SOURCES OF IMPURITIES

The attempt to isolate every potential source of impurities in growth and processing within a number of laboratories utilizing a variety of technologies and procedures is, at best, a difficult task. However, based on the data obtained, we can at least identify some of the areas of commonality and propose potential sources that appear to be the most likely candidates. Since each of the samples examined exhibits its own level of individuality, sources proposed may or may not be applicable equally in all cases.

Sources of impurities include the following:

- o Surfaces
  - a) Retained particulates
  - b) Impurity or cleaning residues
- o Near surface regions
  - a) Drive-in diffusion (polishing, sawing, lapping, etc.)
  - b) Gettered or retained impurities or particulates on remnant damage
- o Starting material purity
- o Stainless steel parts
  - a) Interaction of Hg and/or Te with metal parts
- o Hydrogen flow lines
- o System induced or contributed impurities
- o Feed pot contamination
- o Multiple stirs of melt
- o Precursor gas (MOCVD) purity

- o Stainless steel oven or containment vessels (MBE)
- o Possible mini-oven aperture erosion (MBE)

Although a number of these sources have already been identified, the problem of stainless steel metal part reactivity has emerged in this study as an important factor in impurity introduction in Hg-based alloy growth. Currently, a number of suppliers and independent laboratories are attempting to address this problem by including inert, or reasonably inert, coatings on stainless steel parts. Several labs, both within the United States and Europe, have eliminated stainless parts in mini-ovens.

The problem of surface and near-surface control has been an area that has been addressed in great detail both by the authors and subsequently by other investigators. Although improvements have been made by the industry, the problems still persist. A great deal of money and time has been expended on DoD funded programs to improve or develop new procedures for cleaning surfaces to remove microparticulates and impurities, but evaluation of samples by independent laboratories shows only minimal improvement.

It is recognized that surfaces are not the sole source of impurities in growth technology, but nonetheless, control is needed both for epilayer growth and interface cleanliness prior to passivation of HgCdTe surfaces.

In the sections to follow, we present a brief overview of surface impurity retention and a description of new technology approaches that have been successful for cleaning of binary and ternary compound semiconductor surfaces.

#### 10.0 IMPURITY INCORPORATION AT SURFACES

The topic of impurity incorporation at surfaces or near-surface regions of CdTe, CdZnTe, and HgCdTe is an old one and one that has been addressed extensively by the authors in DoD reports and meetings over the past six years. The sources identified include: (1) particle incorporation during polishing; (2) drive-in distributions during surface finish; (3) contributions from etch/cleaning solutions and subsequent adsorption to surfaces; (4) adherence of impurities to hydrocarbon residues in bonding orbitals or at charge sites

associated with buried subsurface damage or impurity clusters; (5) adherence of secondary or environmentally introduced microparticulates to charge sites at surfaces; and (6) bulk substrate impurities in near-surface regions exposed at the surface by etching or "meltback."

The problem of polishing particle inclusion during surface finish has been largely eliminated with incorporation of longer etching times and final non-contact surface finishing of substrates. The older practice of "contact polishing" of epitaxial layer surfaces is also no longer considered an acceptable procedure for the industry. In current substrates, however, we do still find lower density scattered remnant damage (scratches) remaining as secondary damage with associated impurities along lineated traces.

The introduction of metallic impurities and increased hydrocarbon residues subsequent to chemical etching or cleaning was first reported in distributed DoD reports in 1983. Since this time, a number of labs (both government and commercial) have reproduced this data, albeit lethargically, and attempted to improve surface cleaning procedures. Although some improvement has been noted, the problem remains for both CdTe (CdZnTe) and HgCdTe surfaces. Impurity spiking is noted in discontinuous zones at passivation layer/HgCdTe and epilayer/substrate interfaces. In LPE layer growth, the common tendency has been to increase the meltback time, but this simply results in uneven interfaces and increased incorporation of impurities within interfacial transitional regions. In MBE layer growth, increasing the substrate annealing duration prior to growth does produce some desorption of hydrocarbons and impurities, but in general, bound hydrocarbon chains and impurities are still retained on surfaces. An in-situ cleaning procedure remains as the most advantageous or desirable technique.

#### 11.0 BINDING OF IMPURITIES TO COMPOUND SEMICONDUCTOR SURFACES

A molecule at a free surface is subjected to an attractive potential that determines the nature of interaction. The strength of the interaction is given by  $\Delta H_{ads}$ , which defines the binding energy per molecule. The adsorbed molecules then generally form ordered structures that are dependent on the symmetry of the substrates and chemistry, size, concentration of the adsorbed molecules, as well as the microscopic inhomogeneities of the substrate surface.



For the non-ideal surface or near surface regions of III-V or II-VI semiconductors, the presence of dislocation lines as well as buried impurity clusters ("drive-in" or bulk) contributes to the inhomogeneity of the surface. The presence of remnant or buried residual damage structure in a highly resistive material contributes spatially defined line charge sites via an overlap of space charge regions at the surface. The space charge regions generated around the defect have been shown by the authors to influence oxidation rates, particulate adhesion and impurity attraction to surfaces of compound semiconductors. Native oxide layers or absorbates also contribute to the complexity of the surface behavior. For simplicity, we show in Fig. 57 a cross section of a compound semiconductor surface with an adsorbed organic molecules. The hydrocarbon molecule can bind on the surface either by: (a) hydrogen bonding as a result of the residual dipole-moment of the molecule; or (b) by physisorption resulting from the attraction between charges associated with the molecule and surface atoms.

The attraction of impurities and organics to CdTe or HgCdTe surfaces can be more quantitatively understood from molecular orbital theory. In samples of (111) orientation, the Te atoms on the Te-rich surface retain their  $sp^3$  tetrahedral configuration and can be considered analogous to the nitrogen atom in an ammonia molecule with an unshared pair of electrons as shown below:



AMMONIA MOLECULE

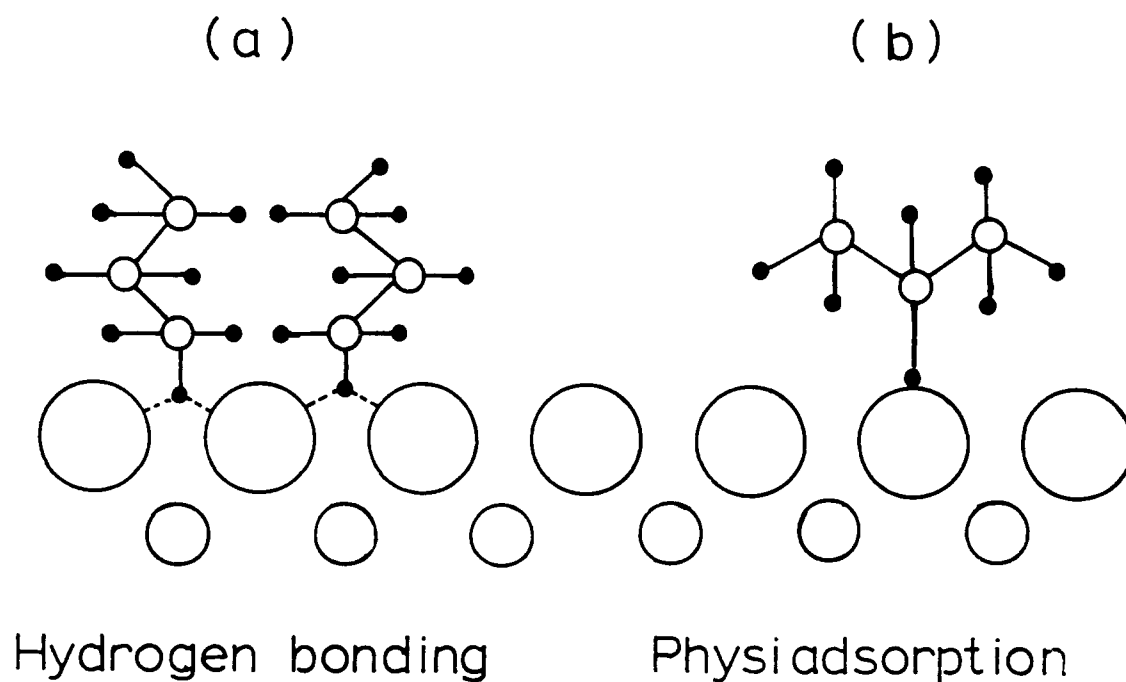


Fig. 57. Simplified schematic showing bonding of organic molecule onto compound semiconductor surface


Conversely, the Te-deficient surface cannot maintain the  $sp^3$  configuration since one of the s-p hybridization orbitals is now unfilled. A planar bond configuration cannot be acquired because the atoms below presumably exhibit tetrahedral bond symmetry. This results in a surface with somewhat distorted tetrahedral bond symmetry.

In contrast, for (100) orientation, only one type of surface exists, since all atoms are either one type or the other. However, the electronic configuration of the (100) surface is expected to be relatively unstable because the unshared electrons (dangling bonds) of surface atoms tend to interact, producing inhomogeneities in charge configuration.

The electronic configuration of Cd, Te, and Hg atoms is shown schematically in Fig. 58. The bonding between hydrocarbon molecules to surface atoms is generally attributed to interaction between  $\pi$  electrons of the molecules and hybrid orbitals of the surface atoms.

The current view of bonding from molecular orbital theory is shown schematically in Fig. 59. The binding between the surface atom and  $\pi$ -orbital consists of two parts: (a) overlap of the  $\pi$  - electron density with a  $\sigma$ -type acceptor orbital on the surface atom; and (b) a "back-bond" resulting from flow of electrons from filled  $sp^3$  hybrid orbitals of surface atoms into antibonding orbitals of carbon atoms in hydrocarbon molecules.

The binding of molecules to semiconductor surfaces can therefore be attributed to the interaction of hybrid orbitals of surface atoms with the  $\pi$  - bonding orbitals of the molecules at the one extreme and to dipole-dipole interaction in the other. The binding will then depend on the type of interaction incurred between surface atoms and adsorbed molecules.

Organic molecules contain certain types of functional groups that exhibit strong affinities for Class II-VI or III-V semiconductor surfaces. Functional groups such as carbonyl,  $>C=O$ , unsaturated carbon double bonds,  $>C=C<$ , and aromatic rings, , show relatively strong interaction due to electrons overlapping bonding orbitals. Conversely, functional groups such as hydroxyls,  $-OH$ , and carboxylic,  $-C(=O)OH$ , show hydrogen like bonding to surface atoms.

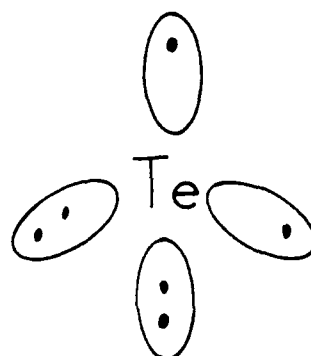
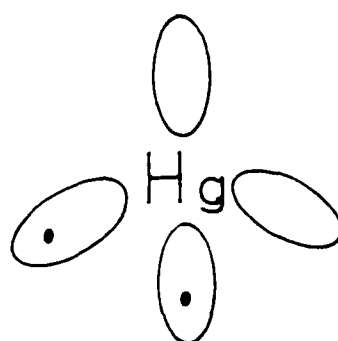
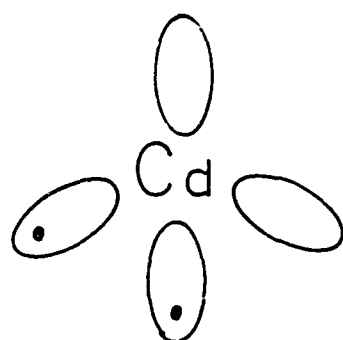
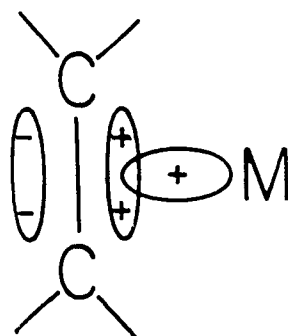
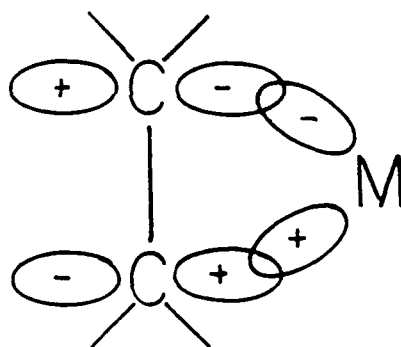


Fig. 58. Electronic configuration of Cd, Te, and Hg atoms



(a)

Donation from filled  $\pi$ -orbitals to vacant surface atom orbital



(b)

Back bonding from filled surface atom orbital to acceptor  $\pi^*$  orbitals

Fig. 59. Schematic showing bonding of molecules to semiconductor surfaces

0080

Polymer molecules, which are normally introduced during chemo-mechanical (intermediate) polishing stages or during final non-contact finishing, contain a rather large number of units or segments, all of which are connected in a single unit. Due to the large molecular size and availability of multiple functional groups of molecules, the surface binding is very effective and traces at surfaces are extremely difficult to remove by conventional cleaning techniques.

In addition to the difficulties presented by trace hydrocarbon retention at surfaces prior to layer deposition and/or passivation, it is the binding of metallics in hydrocarbon regions or directly to surfaces that introduces some of the more serious problems.

## 12.0 BINDING OF METALLICS TO COMPOUND SEMICONDUCTOR SURFACES

Metallic impurities introduced during single preparation or processing steps in the II-VI industry are present in various states. These include metallic oxides, soluble metallic complexes, metal "flakes," and externally introduced contamination in the form of silicates. The binding of metallic impurities to surfaces will then be dependent on the physical and chemical properties of the associated state. In general, the interaction between metallic contaminants and surface atoms follows the behavior of available bonding orbitals of the metal, as well as the surface forces inherited at discrete surface sites.

Transition metal oxide contaminants are the most commonly detected because: (a) they are used in metal parts or glaze coatings of metal parts; (b) they are sufficiently electro-positive to dissolve in acids routinely used for etching of compound semiconductors; and (c) the transition metals have partially filled d or f-shells that allow them to form complexes with ligands. Ligands can stabilize low oxidation states of metal atoms due to the fact that the donor atoms of the ligands possess vacant orbitals in addition to lone electron pairs.

Metal flakes, metallic oxides and silicates can adhere to surfaces via a strong van der Waals interaction or hydrogen bonding, depending on the charge states available at the surface. The presence of a native oxide such as  $\text{Te}_x\text{O}_y$  will facilitate this type of interaction because of charge accumulation and enhanced hydrogen bonding in the presence of residues.

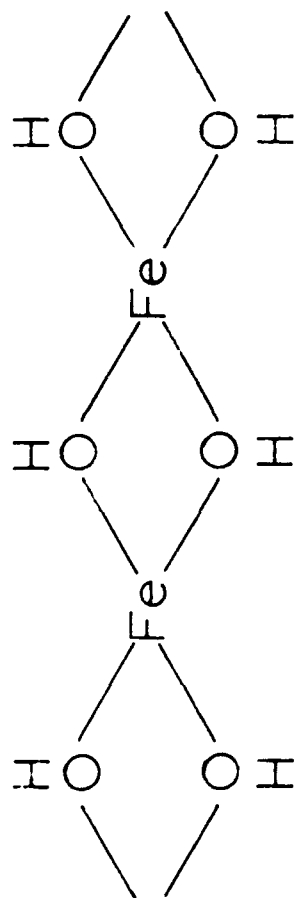
Hydrocarbon traces adhering to compound semiconductor surfaces are normally not effectively removed by conventional cleaning procedures. In the presence of adhering organic molecules with delocalized  $\pi$  - orbitals, such as benzene and unsaturated hydrocarbons, binding of metallic impurities is enhanced, particularly for the d-group transitional metals. In addition, the partially filled d-orbitals of the transition metals have a strong tendency to bind with the  $sp^3$  hybridization orbitals of the surface atoms, particularly when the transitional metal atoms have been stabilized by ligands.

Specific types of surface bonding can be summarized as: (a) overlap of d-orbitals of metal atoms with hybridization orbitals; (b) binding of d-orbitals to delocalized  $\pi$  - orbitals of adsorbed organic molecules on surface sites; and (c) strong dipole-dipole interaction of metallic complexes to localized surface charge sites. To illustrate the bonding mechanisms in more detail, we show schematically in Figs. 60 and 61 the adsorption of  $Fe_2O_3 \cdot nH_2O$  and  $CuO$  onto surface regions. Other transition metals will bind to the surface in similar fashion.

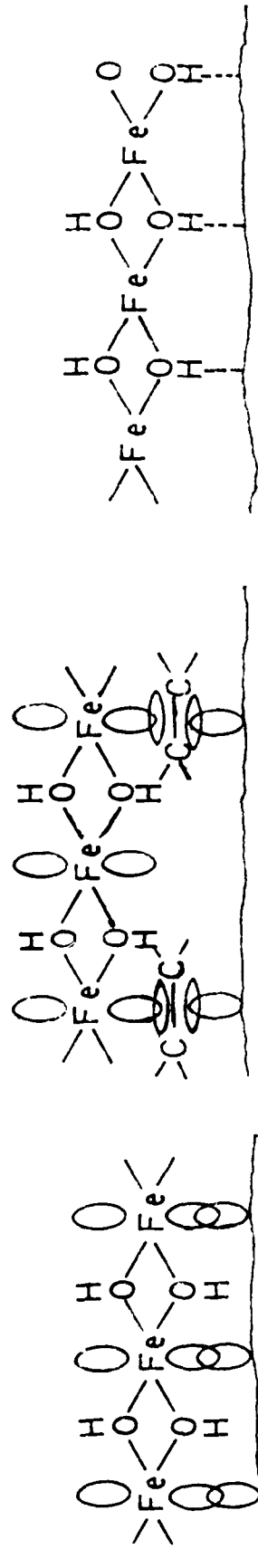
Although the descriptions presented have by necessity been brief, the intent was to discuss mechanisms that would be consistent with experimental data on the adherence of metallics and organic traces to surfaces.

### 13.0 SCANNING UV-LASER CLEANING OF SEMICONDUCTOR SURFACES

Scanning UV laser cleaning has been used on single crystal Si and polycrystalline Si layers at XMR since 1982. Since this time, the procedure has been extended to GaAs, InSb, CdTe, CdZnTe, and HgCdTe. It has been shown to remove hydrocarbon residues, impurities, particulates and native oxides (depending on absorbance). The technique has also now been successfully applied as an in-situ (or in-chamber) cleaning procedure for GaAs surfaces prior to MBE or MOCVD layer growth of GaAs and AlGaAs.



88



SUBSTRATE

(a)

SUBSTRATE

(b)

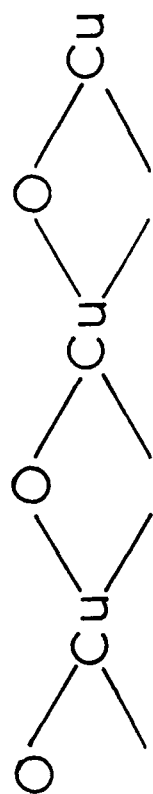
SUBSTRATE

(c)

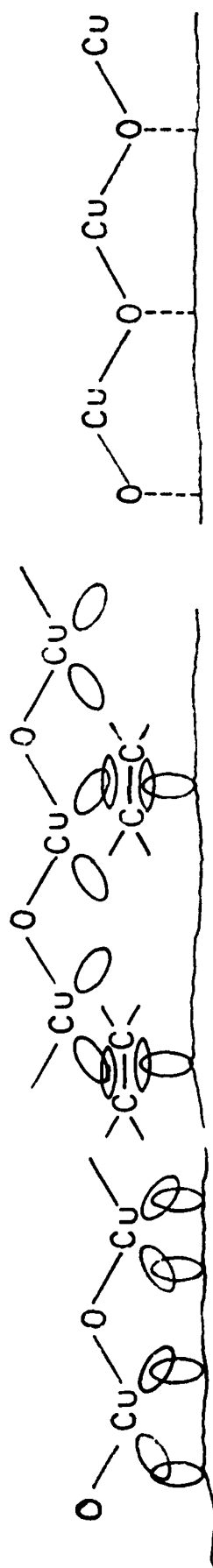
0081

Fig. 60. Bonding of iron oxide to surfaces





CuO



SUBSTRATE

(a)

SUBSTRATE

(b)

SUBSTRATE

(c)

0082

Fig. 61. Bonding of copper oxide to surfaces

The advantages of using UV ( $\lambda = 193$  nm to 308 nm) laser irradiation, in contrast to longer wavelength laser exposure, is in the shallow absorption depth at the surface and the introduction of photochemical and photothermal removal of molecules adsorbed on the surface. In addition, the effective formation of photo-acoustic waves by UV laser irradiation provides sufficient energy to kinetically remove particulates from bound sites on surfaces. Normal UV lamp exposure is ineffective in totally desorbing hydrocarbon residues or oxides and does not remove particulates at all.

The shallow absorption depth in the UV wavelength range for most elemental or compound semiconductors and the low energy densities required for cleaning precludes generation of thermal gradients and damage within near-surface regions. This has been confirmed using RBS, RHEED, TEM, Auger electron spectroscopy and DLTS (Si) measurements.

Hydrocarbon compounds tend to absorb readily in the UV. Bond breaking is achieved at relatively low fluences in the 193 nm to 308 nm range. In Fig. 62, the binding enthalpies of single, double, and triple bonded structures are listed for reference.

In addition, since the latent heat of vaporization is typically in the range, 40-110 kJ/mole, sufficient energy density is available for volatilization of the minute quantities present on surfaces.

Even for high molecular weight organic structures, energy is available to break bonds, giving smaller fragments that can be photothermally vaporized.

Particulates are removed from surfaces by a photo-acoustic effect. Absorption of energy within a shallow region of a semiconductor substrate produces an acoustic wave that is reflected back to the front surface. The acoustic mismatch between the particulate and substrate results in forward momentum transfer to the particle. Since the electrostatic and capillary binding energies of the particle to the surface are small compared to the energy imparted by the acoustic wave, the particle is ejected at measured velocities in the range, 5-10 cm/sec.

Single and Multiple Bond Enthalpies ( $\text{kJ} \cdot \text{mol}^{-1}$ )

Triple bonds	$DH^\ominus$	Double bonds	$DH^\ominus$	Single bonds	$DH^\ominus$	Single bonds	$DH^\ominus$
$\text{N} \equiv \text{N}$	946	$\text{CH}_2 = \text{CH}_2$	682	$\text{CH}_3 - \text{CH}_3$	368	$\text{CH}_3 - \text{H}$	435
$\text{HC} \equiv \text{CH}$	962	$\text{CH}_2 = \text{O}$	732	$\text{H}_2\text{N} - \text{NH}_2$	243	$\text{NH}_2 - \text{H}$	431
$\text{HC} \equiv \text{N}$	937	$\text{O} = \text{O}$	498	$\text{HO} - \text{OH}$	213	$\text{OH} - \text{H}$	498
$\text{C} \equiv \text{O}$	1075	$\text{HN} = \text{O}$	481	$\text{F} - \text{F}$	159	$\text{F} - \text{H}$	569
		$\text{HN} = \text{NH}$	456	$\text{CH}_3 - \text{Cl}$	349	$\text{CH}_3 - \text{NH}_2$	331
		$\text{CH}_2 = \text{NH}$	644	$\text{NH}_2 - \text{Cl}$	251	$\text{CH}_3 - \text{OH}$	381
				$\text{HO} - \text{Cl}$	251	$\text{CH}_3 - \text{F}$	452
				$\text{F} - \text{Cl}$	255	$\text{CH}_3 - \text{I}$	234
						$\text{F} - \text{I}$	243

Fig. 62. Binding enthalpies of single, double, and triply bonded structures

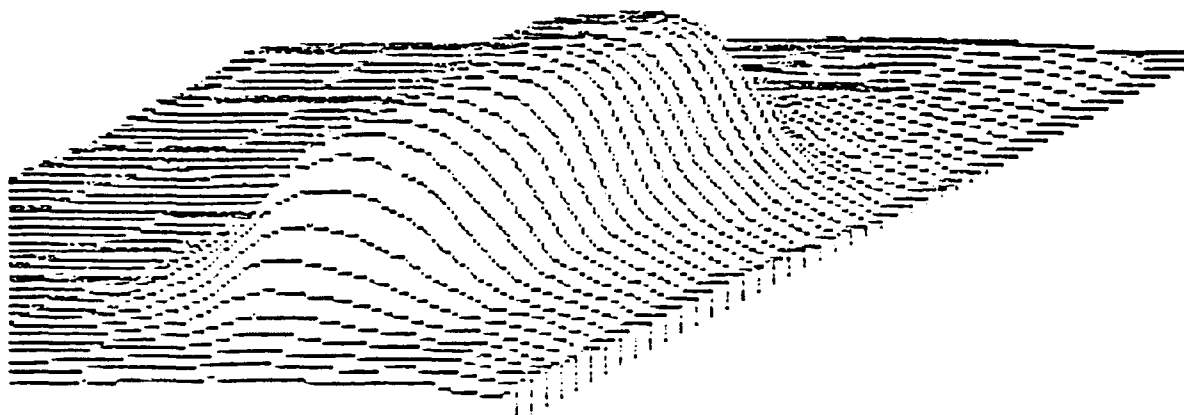
0083

To utilize a UV-laser for cleaning of semiconductors requires that the beam homogeneity be controlled as well as the shot-to-shot stability. To obtain beam uniformity, a multi-element optical homogenizer (patented) was developed by XMR, providing  $\pm 5\%$  uniformity over an irradiation area from 2mm x 2mm to 1 cm x 1 cm. The unit was designed to provide variable aspect ratio in X and Y axis and continuous adjustment over a 1 cm range in either axis.

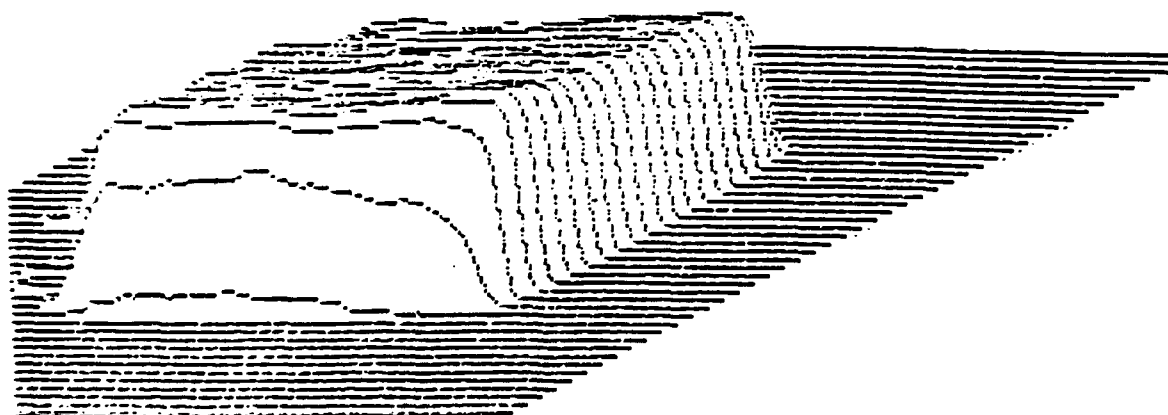
In Fig. 63 are shown the intensity profiles of an excimer laser output beam before and after homogenization. The beam from all excimer lasers shows a spatially varying profile that is not very useful for applications. After homogenization, however, a "top-hat" profile is obtained with sharp abrupt sides and little or no intensity variation across the beam spot area. This type of control is absolutely required for UV-laser enhanced deposition, laser cleaning and other applications.

To provide a clearly defined sample, we deliberately contaminated a CdTe surface with residues and particulates. The sample was then placed in a vacuum chamber and pumped to a level of  $\approx 10^{-6}$  Torr. The surface was then laser scanned in designated areas and removed from the chamber for analysis. In Fig. 64 are shown micrographs of laser cleaned areas adjacent to control or contaminated regions. All particulates and hydrocarbon residues have been clearly removed in the laser cleaned regions. Evaluation by SIMS and ESCA shows no degradation of the surface region and the stoichiometric ratio remains constant. The hydrocarbon, alkali, metallic and tellurium oxide concentrations are substantially reduced or virtually absent, within the detection limits of the ESCA technique.

Similar analysis of less-contaminated surfaces cleaned by conventional procedures shows a reduction or elimination of hydrocarbon and impurity traces as well as complete microparticulate removal. Figure 65 shows superimposed SIMS profiles obtained in an area before and after scanning laser irradiation, illustrating the effective removal of surface contaminants.



1 cm



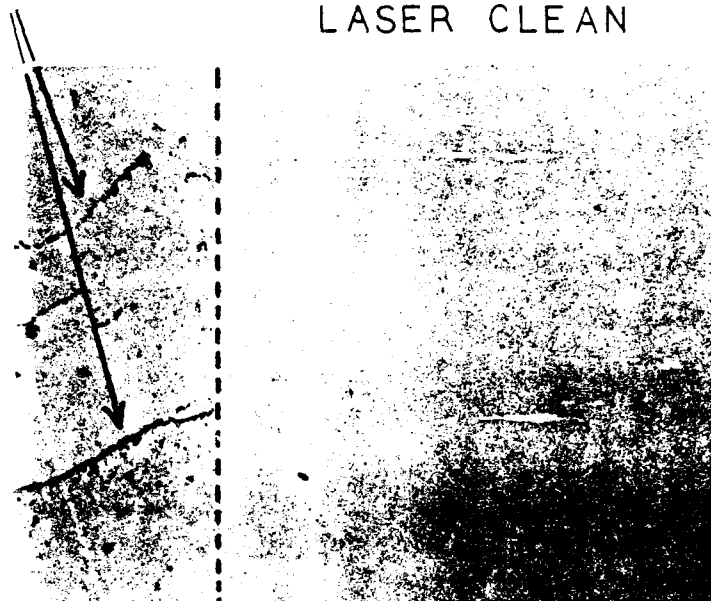
1 cm

Fig. 63. Representative intensity profiles of excimer laser as a function of position before and after homogenization

0084

CONTAMINANTS &  
RESIDUES

LASER CLEAN



$100\mu\text{m}$

Fig. 64. Photomicrograph showing removal of residues  
and particulates on semiconductor surface

0086

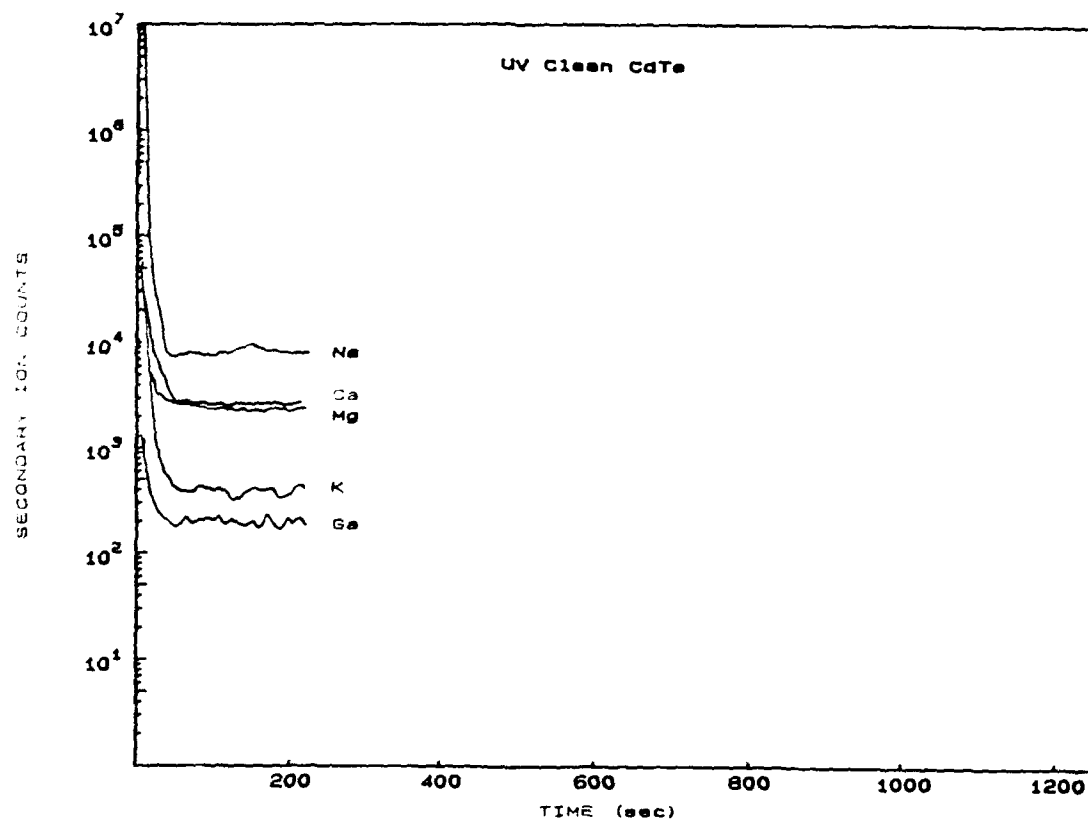
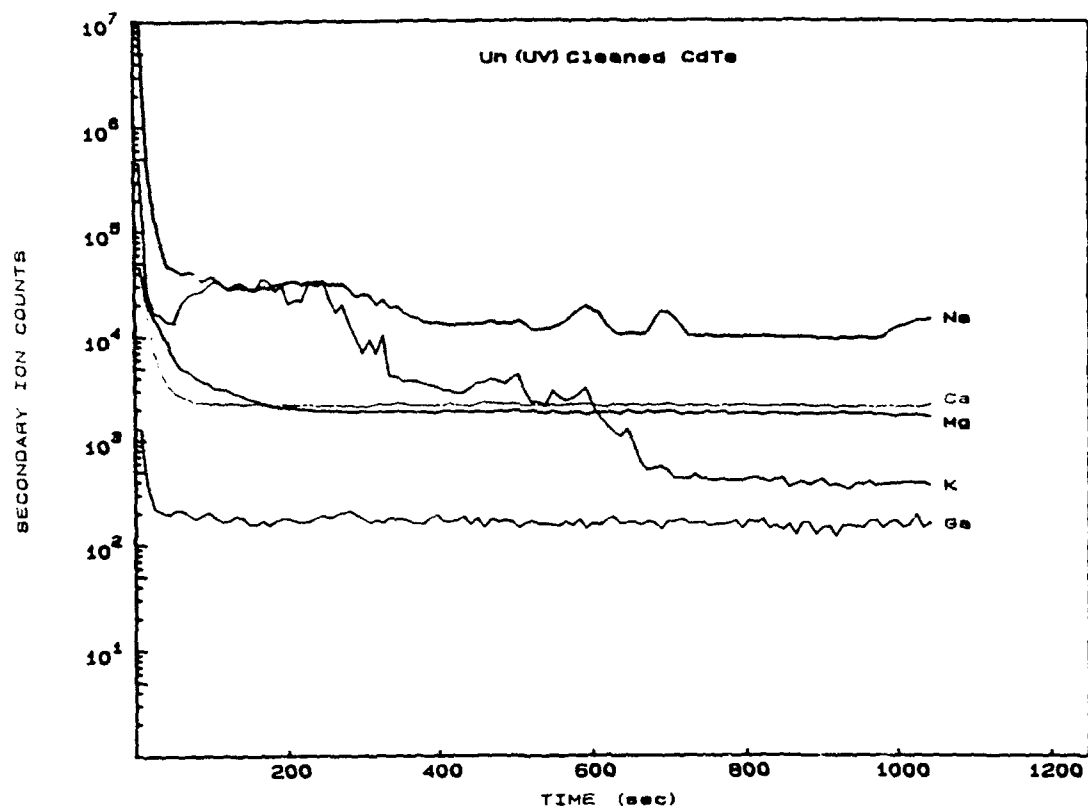


Fig. 65. SIMS profiles obtained on CdTe "before" and "after" UV laser cleaning

0085

#### 14.0 CONCLUSIONS

In the studies conducted over the past two years, we have examined the nucleation of impurity clusters in LPE, VPE, MOCVD, MBE, THM and SSR-HgCdTe material. A wide diversity was found to exist in both the impurity species and concentration of impurity clusters observed in each of these systems. The techniques developed have now enabled identification of the types of impurities introduced during growth and the potential sources.

Surface cleaning procedures used at XMR since 1982 have also been shown to be applicable to CdTe (CdZnTe) and HgCdTe material. Further implementation of these techniques for in-situ or in-chamber surface cleaning should be productive.

A number of questions still remain unresolved, including: (1) kinetics of nucleation; (2) influence of oxygen on nucleation; (3) binding states of impurities; (4) stability of clustered regions; and (5) influence of growth parameters in altering concentration of Te-core site nucleation. The ultimate question, however, is whether the sources of impurities can be eliminated or impurity concentrations can be substantially reduced.

#### 15.0 REFERENCES

1. T. J. Magee and C. Leung, "Subsurface Damage, Near-Surface Impurity Drive-In and Bulk Impurity Clusters in Foreign and Domestic LEC-Gallium Arsenide Wafers,": XMR/DARPA Tech. Rpt. TR-87-1A, (January, 1988).
2. R. A. Sigsbee and G. M. Pound, Advan. Coll. Interf. Sci. 1, 335 (1967).
3. B. Lewis, Thin Solid Films 1, 85 (1967).
4. For more complete discussion, please refer to the following texts:  
  
C. Vidal and A. Pacanlt, editors, Non-Equilibrium Dynamics in Chemical Systems," Springer-Verlag, Berlin, 1984.  
  
N. Wax, editor, "Noise and Stochastic Processes," Dover, New York, 1954.



I. Prigogine, "Introduction to the Theory of Irreversible Processes," 3rd edition. Interscience, New York, 1961.

J. Meixner, editor, "Statistical Mechanics of Equilibrium and Non-Equilibrium," Amsterdam, North-Holland, 1965, p. 80.

-----  
R&D/REP/DARPA2